MANEUVERING OF DISTRIBUTED SPACE-BORNE SENSORS FOR OPTIMAL INTERFEROMETRIC IMAGING PERFORMANCE

A Thesis

by

JULIE SANDBERG

Submitted to the Office of Graduate Studies of
Texas A&M University
in partial fulfillment of the requirements for the degree of

MASTER OF SCIENCE

August 2010

Major Subject: Aerospace Engineering

MANEUVERING OF DISTRIBUTED SPACE-BORNE SENSORS FOR OPTIMAL INTERFEROMETRIC IMAGING PERFORMANCE

A Thesis

by

JULIE SANDBERG

Submitted to the Office of Graduate Studies of
Texas A&M University
in partial fulfillment of the requirements for the degree of

MASTER OF SCIENCE

Approved by:

Chair of Committee,	David Hyland
Committee Members,	John Hurtado
	Takis Zourntos
Head of Department,	Dimitris Lagoudas

August 2010

Major Subject: Aerospace Engineering

ABSTRACT

Maneuvering of Distributed Space-Borne Sensors
for Optimal Interferometric Imaging Performance. (August 2010)
Julie Sandberg, B.S., University of Wyoming
Chair of Advisory Committee: Dr. David Hyland

The need for high resolution, continuously sustained imaging drives the interest in space-borne, distributed aperture, interferometric (amplitude, heterodyne, or intensity correlation) systems. This paper will discuss the maneuver controls for a system of multiple space-based telescopes to secure optimal image quality. Such distributed aperture systems effectively measure the Fourier Transform of the collected light so that the observed wave pattern is seen in the frequency plane. This Fourier Transform representation of physical spacecraft maneuvers may be interpreted as coverage regions (discs) in the frequency plane. Superior coverage of the frequency plane, which is directly related to image quality, is investigated for imaging distant objects using interferometric techniques where apertures are distributed on multiple space-based telescopes. The corresponding cost function is based on the optimality of the spacecraft maneuvers, which in turn is based on achieving a high image quality.

This study builds on previous research wherein the first-order necessary conditions (FONC) were derived. The FONC are derived for specialized rectilinear motion and expanded to incorporate varying coverage disc velocities. These linearized equations are verified to be consistent with those for the constant velocity case. Next, linearized first-order necessary conditions are shown to correspond closely with the fully nonlinear case. After that, the conditions for optimal overlap of the coverage paths will be given; these conditions lead to the optimal cost based on frequency plane parameters. Finally, a heuristic approach will be used to compare different frequency

plane coverage strategies. An analogy to painting will be presented to demonstrate adequate signal-to-noise ratio required for a desired image quality.

ACKNOWLEDGMENTS

I would like to thank my adviser, Dr. David Hyland, for all the support and advice he has given me throughout my time as a graduate student. I have enjoyed working with him, and I am thankful to have had such a great adviser. In addition, I would like to thank my professors who have helped me throughout the years and helped guide me to where I am today.

I would like to thank my sister, Lori, for her patience and enouragement. To my parents I owe many years of discipline and encouragement; I could not have made it through a rigorous engineering program otherwise. They taught me to work hard and to never give up.

My friends and family have also been an inspiration to me. Thank you for always encouraging me.

Last, but definitely not least, I would like to thank Tim for always being there for me. He understands me better than anyone else, and he has been very understanding with me throughout my research.

TABLE OF CONTENTS

CHAPTER Page

LIST OF FIGURES

FIGURE Page

CHAPTER I

INTRODUCTION AND RELATED WORK

The physics behind multi-spacecraft interferometry is the driving factor in obtaining quality images. Though the method of using multiple spacecraft to image distant objects has been studied, an optimal solution for covering the frequency plane has not been found. Also, the spacecraft dynamic requirements as they relate to an optimal coverage solution has not been investigated [1]. Frequency plane coverage, based on image quality and signal-to-noise ratio, is directly related to the dynamics and aperture characteristics of all spacecraft.

This study investigates optimal image formation, a concept that is used to describe a desired signal-to noise ratio (SNR) as well as other image parameters. As will be discussed, these techniques focus primarily on image quality rather than on the physical motion of the spacecraft apertures. The relative motion of the spacecraft may then be determined based upon achieving a high resolution image. The objective of this study is to investigate specialized cases within the optimal imaging problem, a challenging area of research that requires substantial work before a completely optimal solution will be obtained. As a result, researchers have examined a variety of specific aspects of the topic. Other studies focus on optimal fuel usage, time, or additional physical parameters that are important when considering the imaging of distant objects; however, these considerations are secondary in the current study. Selected similar investigations may be found in [2, 3, 4]. Some studies, such as [3] also consider a noise model, though the impact of noise on the system is beyond the scope

---

The journal model is *IEEE Transactions on Automatic Control.*

of this study.

A driving factor in imaging is resolution. The imaging capacity of a telescope is quantified by the angular resolution it is capable of distinguishing. The angular resolution is the angular distance between two objects such that the telescope can distinguish them as separate entities. In general, larger optical telescopes have a higher capability of angular resolution. Creating large apertures, however, is a technical challenge. To achieve a higher angular resolution and also a higher sensitivity, space-based telescopes are the design of choice. Generally, launching costs increase with mass, which is a limiting factor in the size of space-based telescopes. Another limiting factor in space-based telescopes is the size constraint resulting from the launch vehicle payload dimensions [5]. Some telescopes may deploy after release from the launch vehicle, but this technique leads to alignment constraints. A popular strategy is to coordinate multiple telescopes and combine the light collected to form a single image using the method of interferometry [6]. Other technology fields have recently begun implementing sets of smaller satellites in place of a single, large satellite for non-interferometric methods because of the improvements in mass, volume, power consumption, and performance. In addition, the malfunction or loss of a single satellite does not necessarily result in mission failure [7].

Interferometric imaging of distant objects such as planets beyond our solar system, stars, or black holes has been a topic of much consideration. Searching for the presence of life on distant planets is of scientific and philosophical interest. In recent years, scientists and engineers have been developing technology that allows for direct observation of remote worlds [5, 8]. Other applications requiring a high image resolution include Earth observation. Formation flying, a specific example of distributed space systems, allows for the method of interferometry by requiring multiple spacecraft to maintain a precisely coordinated configuration and combine

the light from all apertures to form a single image. Additional forms of distributed space systems include swarms, constellations, and inspection & docking as described in [7]. A constellation typically requires no active control, while formation flying is dependent upon active control to meet position and velocity requirements. Swarms, composed of hundreds or thousands of satellites, have not yet been fully developed. Formation flying is the chosen superior method in the present imaging study as its application allows for advanced angular resolution. Guidance, navigation, and control subsystems are critical to formation flying mission success because the relative distances between spacecraft must be precisely controlled [5]. Examples of formations include several NASA satellites: Aqua studying Earth's atmospheric and oceanic climates, Aura studying Earth's ozone and air quality, and CloudSAT studying clouds worldwide [9].

Formation flying reconfiguration maneuvers are essential for achieving mission goals. These maneuvers must occur within a predefined time period and may include resizing of the formation, slewing or re-targeting, or rotation of the formation about the interferometric bore sight. Fuel expenditure is the driving factor in optimal spacecraft maneuvers [10]. As observed in [11], the point about which a formation rotates determines the amount of fuel consumed by each spacecraft. For instance, if one spacecraft is chosen as the inertial point, it will not require fuel for the maneuver, leading to an uneven distribution of fuel among the constituent spacecraft. A number of autonomous control schemes have been developed to implement spacecraft formation maneuvers, and further information may be found in references such as [12, 13, 14].

Interferometric methods involving entry pupil processing (EPP) convert the collected light into digital signals for analysis. This technique relaxes the formation control precision constraints and the necessity for merging the light in a centralized

combiner. Controlling optical path differences is of less concern for EPP. In essence, the spacecraft may operate as an independent system, though it must gather position knowledge corresponding to imaging data [15].

A. Overview

Interferometry using afocal telescopes is the method used throughout this paper. When light passes through separate apertures, the collected light is combined to form an interference pattern that is the Fourier Transform of the combined light [16]. As a result, it is of utmost importance to note here that the image quality analysis is performed on the Fourier Transform of the collected light, which is represented in the frequency plane. Therefore, most equations describing the optimal imaging problem will be described in the frequency plane rather than the spatial plane. The figure on page 14 shows the relationship between these two planes; the images resulting from the prescribed interferometry technique may be obtained by taking the Inverse Fourier Transform (IFT) of the collected light. Small measures of signal inadequacy in the frequency plane result in a degrading of the imaging system. However, this study does not involve image processing of the collected light and assumes complete interferometric measurements that have not been obscured by noise.

In Chapter II, basic optical concepts relevant to the study will be described. Additionally, the relationship between the physical and frequency planes will be emphasized and illustrated. Chapter III will give an overview of several of the findings of [2] and explain their foundation for the present study. Next, Chapter IV will outline the problem formulation. The derivation for time-dependent velocity equations in the specialized rectilinear case will be presented. Also, the first order necessary conditions will be linearized and discussed. A metaphor using a painting process will be used

to portray the implications of frequency plane coverage as it relates to signal-to-noise ratio and image quality. This metaphor will be expanded to include a thin paintbrush analogy used to describe an instantaneous velocity solution. Chapter V will present and summarize the results obtained using various simulations in Matlab. These results will be compared and contrasted with the previous work given in Chapter III. Lastly, conclusions and future work that would build upon the results of this study will be described in Chapter VI.

CHAPTER II

BASICS OF INTERFEROMETRIC IMAGING

This chapter introduces the basic concepts of imaging, then expands these concepts to include a multi-spacecraft imaging configuration with lens-less apertures.

A. Basics of Optics and Optical Imaging

Optical interference has been observed for over a hundred years through various laboratory experiments. When two light waves exhibit slightly different optical path lengths, they produce an interference pattern. A small path offset affects the light wave interactions noticeably because visible light has a very small wavelength. As will be discussed, this interference due to the variation in wave properties, allows for the powerful application of interferometric imaging.

1. Mathematical Representation of Waves

It is well known that electromagnetic waves consist of an electric vector and a magnetic induction that depend upon one another for propagation through space [16]. As a result, only a single field must be considered in order to know the properties of the other. Usually the electric field is observed, which is a time-varying vector perpendicular to the direction of the wave propagation. The relationship

$$E(x, y, z, t) = a\, cos\left[2\pi\left(\nu t - \frac{z}{\lambda}\right)\right] \tag{2.1}$$

is used to describe the electric field at a point in the spatial domain (x, y, z) resulting from a plane light wave propagating along the z-axis, where a is the amplitude of

the light wave, ν is the frequency, and λ is the wavelength. For a point source, as is the case for many distant objects, light radiates uniformly in all directions and the wavefront can be represented as a time-dependent expanding sphere. This spherical wave is described as a function of the sphere's radius and time:

$$E(r,t) = \left(\frac{a}{r}\right) cos\big[\omega t - kr\big] \tag{2.2}$$

When the point source is distant, a small area of the spherical wavefront can be approximated by a plane wave [17].

Though equations (2.1) and (2.2) are written in terms of a cosine function and are visually meaningful, for mathematical manipulations it is more practical to represent a plane wave using complex exponential terms as in

$$\mathbf{E}(\mathbf{x},t) = \hat{\mathbf{s}} E_o e^{\left(i(-\omega t \pm \mathbf{k}\cdot\mathbf{x}+\phi)\right)} \tag{2.3}$$

In this equation, $\hat{s}$ represents the transversal component of the wave, the wave number $k = \frac{\omega}{c} = \frac{2\pi}{\lambda}$, and ϕ is the phase [1]. A more general representation of equation (2.3) is the Maxwell equation, where c is the speed of the wave and λ is the wavelength of light:

$$\begin{aligned} \nabla^2\mathbf{E} &= \frac{1}{c^2}\frac{\partial^2\mathbf{E}}{\partial t^2} \\ \nabla\cdot\mathbf{E} &= 0 \end{aligned} \tag{2.4}$$

For this representation of an electromagnetic wave, the polarization of the light is not taken into account and the equation is true for any transversal component of the wave.

2. Introduction to Wave Interference

Two waves that have been superimposed add constructively or destructively to produce a pattern of fringes. Figure (1) demonstrates this phenomenon. If the waves are parallel spatially and temporally, they are said to be coherent; if they line up partially and do not exhibit total destructive interference, they are considered partially coherent.

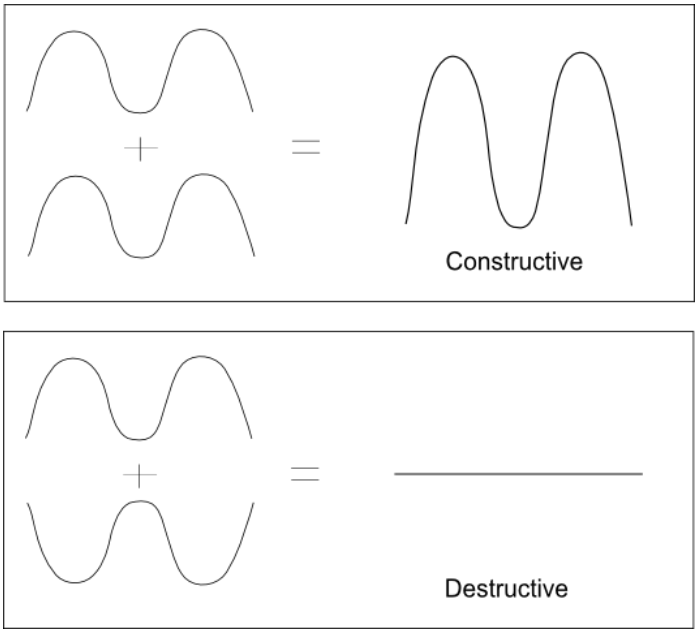

Fig. 1. Interference of two waves

A famous two-slit experiment performed by Thomas Young irrefutably demonstrated that light has wave-like properties. Figure (2) shows a diagram of this experiment, which consisted of a light source, a single slit mask closest to the source, a double slit mask in the middle, and a screen to record the interference pattern from the two slits.

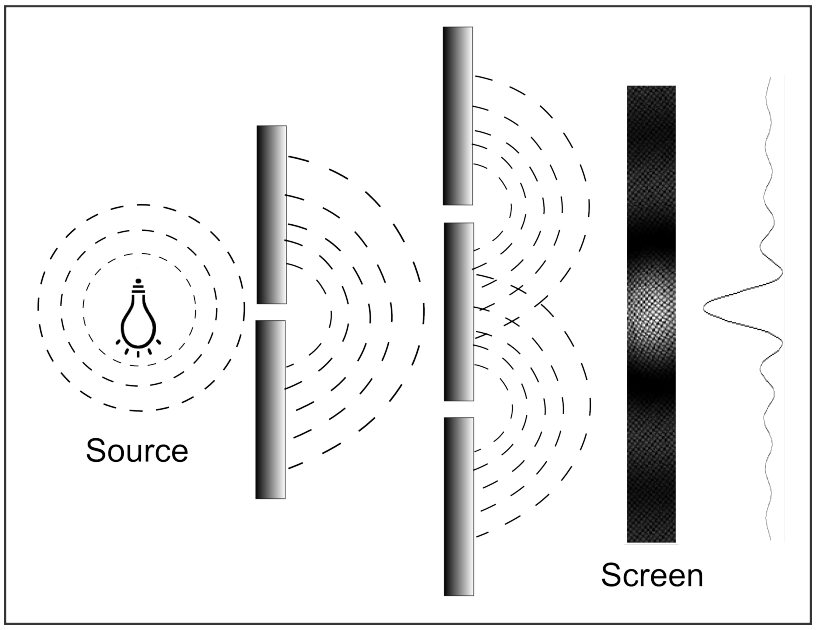

Fig. 2. Young's double slit experiment

This two-slit experiment shows how the source light traveling through the single slit, acting as a single point source, is split into two nearly identical light sources. These two light sources, having spherical wavefronts, are then projected onto the screen in a sinusoidal pattern. Larger magnitudes of the resulting sinusoid occur where the light interferes constructively. The complex amplitude of the two waves can be represented by

$$A = A_1 + A_2, \tag{2.5}$$

while the resultant intensity is given by

$$\begin{aligned} I &= |A|^2 \\ &= (A_1 + A_2)(A_1^* + A_2^*) \end{aligned} \tag{2.6}$$

In general, $A_1 = a_1 e^{(-i\phi_1)}$ and $A_2 = a_2 e^{(-i\phi_2)}$ [17, 18].

The fringe spatial frequency with regard to the intensity distribution on the screen is proportional to the baseline b; in this case, the slit separation is measured in units of the wavelength λ. The mathematical description for this frequency is given by

$$F_{SF} = \frac{b}{\lambda}\theta^{-1} \tag{2.7}$$

Similarly, the fringe spacing can be determined by

$$F_S = \frac{\lambda}{b}\theta. \tag{2.8}$$

where θ is the resolving angle [2]. The intensity of an interference pattern has a maximum value, given as

$$I_{max} = I_1 + I_2 + 2(I_1 I_2)^{1/2} \tag{2.9}$$

when the phase difference is $\Delta\phi = 2m\pi$. The intensity has a minimum value of

$$I_{min} = I_1 + I_2 - 2(I_1 I_2)^{1/2} \tag{2.10}$$

when the phase difference is $\Delta\phi = (2m+1)\pi$. In both cases, m is an integer.

A monochromatic point source, meaning that all light waves emitted share the same amplitude and linearly-varying phase, results in evenly spaced, well-contrasted

fringes. However, when an extended monochromatic source with slightly-varying amplitudes and phases is used, fringes exhibit clear contrast only in a certain region. This effect is known as fringe localization and is due to inadequate spatial coherence of the illumination. The concept of coherence will be further described in the next section. A quality of the interference fringes, called the visibility or fringe visibility, is defined [17] as

$$\nu = \frac{I_{max} - I_{min}}{I_{max} + I_{min}} \tag{2.11}$$

For an ideal point source, the light is completely coherent, resulting in a fringe visibility of unity.

When imaging an optical field, knowledge of the wave amplitude and phase leads to an understanding of the fringe pattern and a description of the object under consideration, concepts that are described in the following sections.

B. Basics of Coherence Theory

Coherence describes the similarity between waves both in time and space. This quality is related to whether waves interfere constructively or destructively. For a monochromatic source, the electric field is by definition coherent. For other more common sources, light with varying amplitudes and phases may only be partially coherent. The coherence yields a value of the visibility for the interference fringes [17]. Source waves may have temporal coherence when considering a finite bandwidth or spatial coherence for a finite area of space [18]. Waves of the same frequency are considered to be mutually coherent if they have a constant phase during a given time period, and a mutual coherence function gives a cross-correlation between light at two different observation locations [16]. Point sources having mutually uncorrelated phase may be

defined as an extended incoherent source [2].

1. The Huygens Fresnel Principle

In 1690 Christiaan Huygens, a Dutch mathematician and scientist, published a principle that was later named after him. It states that at each point in a traveling wavefront, each element serves as the source of a set of spherical secondary wavelets. These secondary wavelets have the same frequency and speed as the original propagating wave at the reference point, and the position of the wavefront consists of all wavelets [16]. The shape of the wavefront, or any portion of the wavefront, is the envelope of the secondary wavelets, regardless of wavelength [18].

In the 1800s, French physicist Augustin-Jean Fresnel adapted the Huygens Principle to include the effects of mutual interference [16]. The Huygens-Fresnel Principle states that at any point considered to be the source of infinitesimal secondary wavelets, the amplitude of the optical field is the superposition of these wavelets' amplitude and phases [18]. According to this theorem, the pattern resulting in light passing through an aperture is the spatial Fourier Transform of the aperture shape; the electric field can be reconstructed from the collected light by taking the Inverse Fourier Transform. The next section gives mathematical formulae for and the relationship between the Fourier Transform and Inverse Fourier Transform.

a. Relationship Between Spatial and Frequency Planes

The two-dimensional Fourier Transform (FT) of light, F', is defined in the frequency plane (p, q) to be

$$F'(p,q) = \int_{y=-\infty}^{\infty} \int_{x=-\infty}^{\infty} F(x,y) e^{2\pi i(px+qy)} dxdy \tag{2.12}$$

while the Inverse Fourier Transform (IFT), F, is defined in the spatial plane (x, y) as

$$F(x,y) = \int_{q=-\infty}^{\infty} \int_{p=-\infty}^{\infty} F'(q,p) e^{-2\pi i(px+qy)} dpdq \tag{2.13}$$

The IFT of the light collected from the apertures in the frequency plane is therefore represented in the two-dimensional spatial plane [19].

Figure 3, adapted from [2], shows the relationship between the physical plane and the frequency plane using multiple apertures and a very long baseline configuration, where the apertures are separated at a relatively large distance and assumed to image the same source over the same time period. Here, the angular resolution is defined by Rayleigh's Criterion,

$$\theta_R = \frac{\lambda}{D} \tag{2.14}$$

where λ is the wavelength and D is the diameter of the aperture. The angular resolution is the smallest value such that two closely positioned objects are detected as separate sources. For an extended incoherent source, the angular resolution is calculated for all ranges of observed wavelengths.

Note, from Figure (3), that the largest feature in the spatial plane (i.e., the entire object or scene to be imaged) corresponds to the smallest resolvable feature in the frequency plane. If the Fourier component is measured at $(\vec{\chi}_m - \vec{\chi}_n)/\lambda$ in the frequency plane, some Fourier component value may be ascribed to the entire neighborhood of diameter $1/\theta_P$ about $(\vec{\chi}_m - \vec{\chi}_n)/\lambda$. Therefore, because of the finite size of the picture frame, each interference measurement establishes a coverage disc in the frequency plane wherein the Fourier coefficient is fully specified.

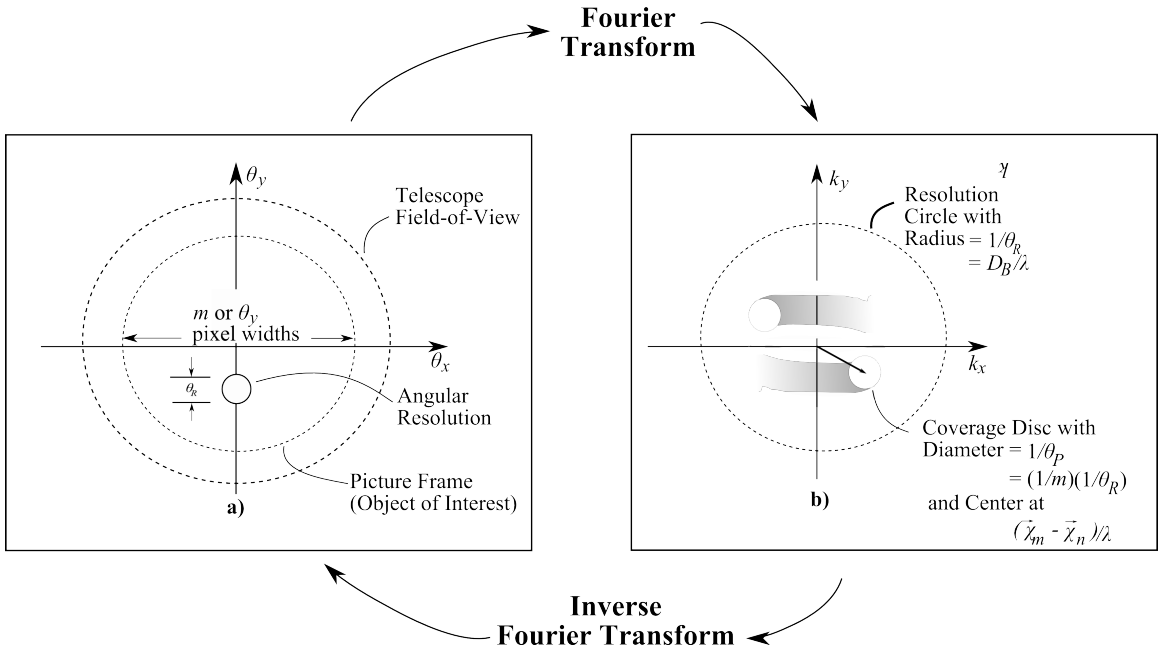

Fig. 3. Relationship between regions in spatial plane (left) and frequency plane (right)

Figures (4) and (5) show the coverage discs and the corresponding physical spacecraft locations at the beginning of the Matlab simulation used to generate results for Chapter V. During the simulation, $N(N-1)$ coverage discs move within the resolution plane, where N is the number of apertures [2]. Note that, due to the symmetric nature of the frequency plane, only $\frac{N(N-1)}{2}$ coverage discs exist. The additional coverage discs are mirrored about the origin; the frequency plane is symmetric, meaning $F(x,y) = F(-x,-y)$ [20].

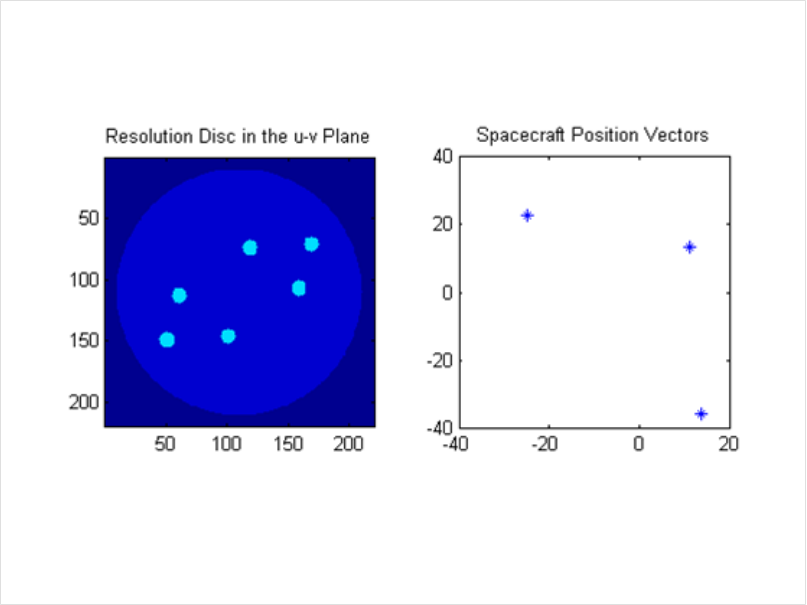

Fig. 4. Matlab simulation of coverage discs in frequency plane (left) and spacecraft physical (non-dimensionalized) locations for N = 3 (right)

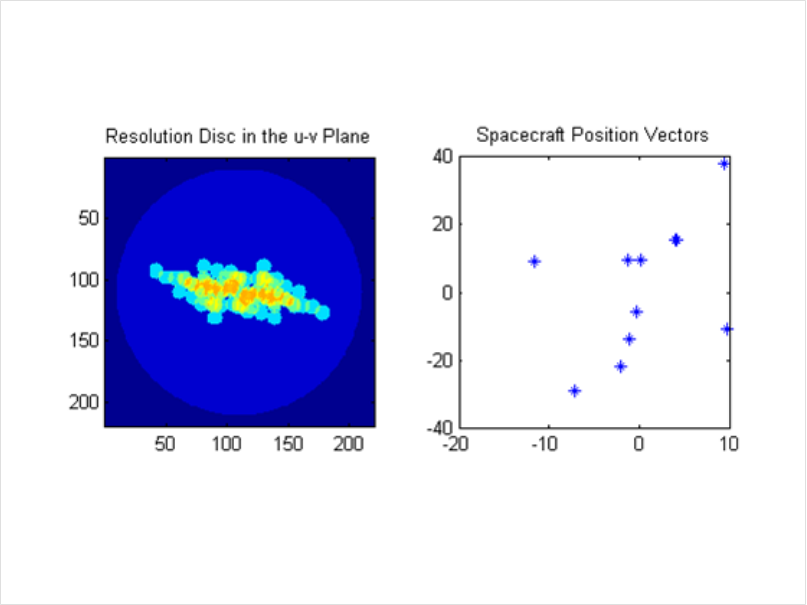

Fig. 5. Matlab simulation of coverage discs in frequency plane (left) and spacecraft physical (non-dimensionalized) locations for N = 10 (right)

2. The Helmholtz Equation

The scalar description of an electromagnetic field along the x-axis is

$$U(\mathbf{x},t) = E_o e^{-i\phi} e^{\left(i(-\omega t \pm \mathbf{k}\cdot\mathbf{x})\right)} \tag{2.15}$$

Let $U(\mathbf{x},t)$ be one scalar component of the electric field. Taking the Fourier transform of U results in

$$\hat{U}(\mathbf{x},w) = \int_{-\infty}^{\infty} U(\mathbf{x},t) e^{(-iwt)} dt \tag{2.16}$$

When considering only a narrow bandwidth Δw, U is the average value of the field over a small variation of the frequency centered about Δw, such that

$$U(\mathbf{x}) = \bar{U}(\mathbf{x},\bar{w}) \tag{2.17}$$

When Δw is much smaller than the center frequency, $U(\mathbf{x},t)$ is said to be quasi-monochromatic. In such a case, $U(\mathbf{x})$ is a solution to the Helmholtz Equation [1]:

$$(\nabla^2 + k^2)U = 0 \tag{2.18}$$

3. Helmholtz-Kirchoff Integral Theorem

Huygens and Kirchoff derived an equation describing a field propagating outward from a single, extended incoherent source, which consists of several independent point sources that generate separate fringe patterns. Figure (6) shows an example of simple image-acquiring geometry from [3], which models this description. Q is any point on the image surface, point P lies on the observation surface, which is very distant from the source, and n_P and n_Q are unit vectors normal to their respective surfaces. The

wavefront from the source spreads as it travels in a spherical shape; full knowledge of U and $\frac{\partial U}{\partial n}$ is assumed. The image surface lies on or near the source; light first passes this image surface, then travels through the observation surface. The apertures will lie essentially on the observation surface, though in certain configurations they may be located at small distances from the plane along the z-axis [2].

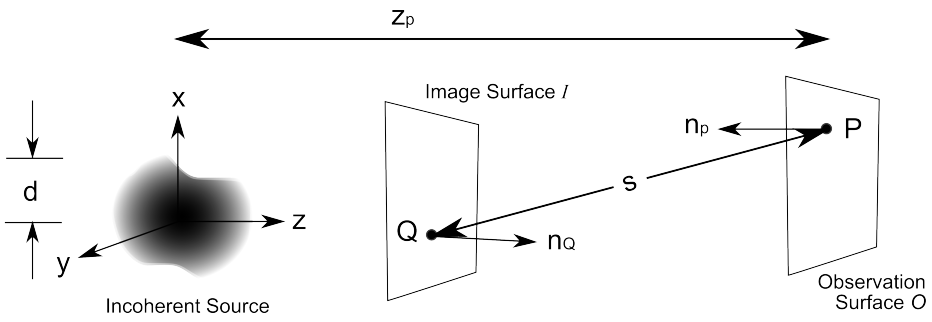

Fig. 6. Geometry of basic imaging

The mathematical formula for the scenario described in Figure (6) as devised by Helmholtz and Kirchoff is

$$U(P) = \frac{1}{4\pi} \int_I \left\{ U(Q) \frac{\partial}{\partial n_Q} \left(\frac{e^{iks}}{s} \right) - \frac{e^{iks}}{s} \frac{\partial U(Q)}{\partial n_Q} \right\} dQ \tag{2.19}$$

where dQ is a differential element on the image surface. This equation assumes steady conditions of the light source on the image and object planes.

Because of a time reversibility property of light propagation, an exact inverse relationship may be found for equation (2.19). The path of the light traveling in a spherical shape from the source may be reversed in time so that the light may be considered to originate from the observation plane and pass through the image plane,

finally converging at a point in the center of the spherical wavefront.

To mathematically describe the phenomenon on time-reversal light propagation, simply replace t in equation (2.19) with $-t$ [2]. This results in

$$U(Q) = \frac{1}{4\pi} \int_O \left\{ U(P) \frac{\partial}{\partial n_P} \left(\frac{e^{-iks}}{s} \right) - \frac{e^{-iks}}{s} \frac{\partial U(P)}{\partial n_P} \right\} dP \tag{2.20}$$

Using this integration formula, inverse propagation of the light waves results in complete knowledge of the electromagnetic field of the source. This information is useful in determining the coherence of the object.

The Huygens-Fresnel Principle states that the light passing through an aperture is the FT of the aperture shape; from this frequency plane representation of the image, the electric field can be reconstructed. Then, given mutual coherence measurements on the observation surface, the image intensity can be reconstructed according to the Van Cittert-Zernike Theorem [16]. The van Cittert-Zernike Theorem gives a relationship between the complex degree of coherence in a region of space and the irradiance across an extended source [18].

C. Basics of Interferometry

Interferometers are based on the same principles examined in Young's two-slit experiment, as shown in Figure (2). Measurements of a light source are made to interfere: two separate beams are used; one serves as the reference and the other is the test or measurement. The optical path difference between these wavefronts is described by [17] as

$$\begin{aligned}\Delta p &= p_1 - p_2 \\ &= \Sigma(n_1 d_1) - \Sigma(n_2 d_2)\end{aligned} \tag{2.21}$$

Examples of hardware used to interfere two beams from the same light source include the Michelson Interferometer, Separate Element Interferometer, Mach-Zehnder Interferometer, and the Sagnac Interferometer. The concepts and descriptions of these interferometers may be further researched using any basic optics textbook or reference. All of the aforementioned instruments use optical techniques to physically combine the beams and produce a result.

The optical intensity interferometer was developed for radio astronomy by R. Hanbury Brown to generate measurements of starlight more precisely than previous methods would allow. During that period of time, angular measurements were not very accurate, due in part to the fluctuations in the Earth's atmosphere. The optical intensity interferometer was revolutionary in the fact that it combined the beams electrically.

Figure (7), adapted from [21], shows a simple schematic of Brown's optical intensity interferometer where P_1 and P_2 are photo-electric detectors and f_1 and f_2 are wideband filters. The filters select the wavelengths of interest as input to the correlator. The correlator then multiplies the resulting two voltages and measures their average over a given time period. This product is called the correlation between the two detectors. If the light from a single source is coherent at two separate measurement points, there is a correlation between the fluctuation of the intensities at these same points. The normalized correlation is proportional to the square of the degree of coherence and to the square of the fringe visibility.

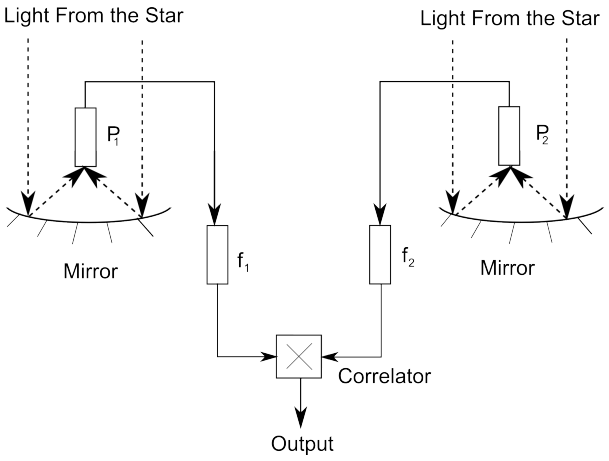

Fig. 7. Optical intensity interferometer

The robustness of the optical intensity interferometer stems from the fact that it does not require stringent mechanical precision for very long baselines. In addition, it is not drastically affected by atmospheric disturbances [21].

1. Two-Beam Interferometry

Fringe patterns may be produced when two coherent beams are interfered. If light from a single source is used for both beams, coherence is achieved by definition. Two methods are commonly incorporated to generate interference patterns: wavefront division and amplitude division. Wavefront division isolates one beam from the detected wavefront and one beam from an optically derived secondary wave, while amplitude division splits beams from the original wavefront. Examples of each type of interferometer include the following:

Wavefront Division Interferometers

- Young's Experiment

- Fresnel's Double Prism
- Lloyd's Mirror

Amplitude Division Interferometers

- Michelson Interferometer
- Mach-Zehnder Interferometer
- Sagnac Interferometer

2. Multiple Beam Interference for Sparse Aperture Systems

Better image resolution is achieved with multiple entry pupils than that which is possible by a single telescope used to image a distant light source. Consider these pupils for the ideal imaging scenario. Here, N circular apertures are used, each with diameter D_T. Let x_P be the location of the x^{th} pupil and τ be a generic term describing the time period over which imaging takes place. The Aperture Function is defined as the total aperture area over the image acquisition period:

$$A(\vec{x}_P, t) = \sum_{k=1}^{N} A_T(\vec{x}_P - \vec{x}_k) \tag{2.22}$$

where $\vec{x}_P$ is the position of an arbitrary point in the physical plane, $\vec{x}_k(t)$ is the position of the k^{th} aperture, and in general, A_T is

$$A_T(x) = \begin{cases} 1 & \text{for } |x| \leq D \\ 0 & \text{Otherwise} \end{cases} \tag{2.23}$$

The image intensity is described as

$$I_T(\vec{\theta}) = \int d\vec{\theta_1} \left| \Lambda(\vec{\theta} - \vec{\theta_1}) \right|^2 I(\vec{\theta_1}) \tag{2.24}$$

Here, λ is the wavelength, and the look angle vector, $\vec{\theta}$, is defined as the angle between the surface normal to the image plane and the source under consideration. Referring to the basic imaging scenario in Figure (6), for an object at distance $(0, 0, z)$ [2]

$$\Lambda(x_Q, y_Q) = \frac{1}{\lambda z}^2 \int dx_P \int dy_P A(x_P, y_P) e^{2\pi i \frac{1}{\lambda z}(x_P x_Q + y_P y_Q)} \tag{2.25}$$

3. Modulation Transfer Function

Modulation refers to the normalized amount a function varies from its mean value [18]. The modulation transfer function (MTF) describes the how closely a reconstructed image represents the source. This characteristic of the imaging system's performance is the ratio of the estimated image intensity to the true intensity. A larger value of the MTF indicates that taking the IFT of the collected signal will generate a restored image that is close to the true image. The MTF depends on both the apertures and the configuration of all spacecraft [3]. The MTF is the convolution of the aperture functions, defined in equation (2.22), as measured from all spacecraft in the frequency plane. The current study neglects the effects of noise on the MTF.

4. Point Spread Function and Optical Transfer Function

The impulse response of an imaging system may be determined by observing a point source. Because of diffraction resulting from light bending as it passes through the aperture, the imaged object will result in a blurred image rather than a clear point. This spread of the imaged point indicates the quality of the imaging system and is called the Point Spread Function (PSF).

The Optical Transfer Function (OTF) is the Fourier Transform of the PSF; its modulus is the MTF while the phase is called the Phase Transfer Function. Figure (8) shows an example of a Gaussian PSF and its corresponding MTF.

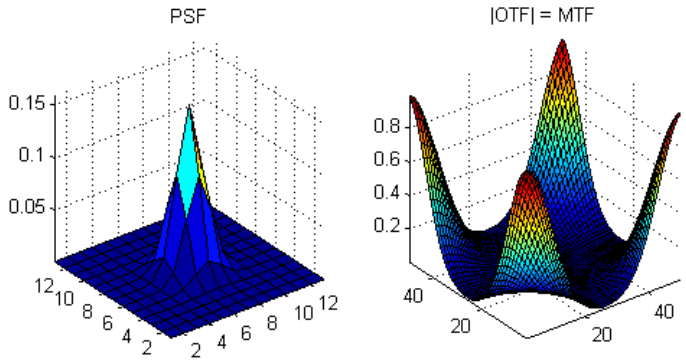

Fig. 8. Relationship between point spread function and modulation transfer function

a. Summary

This chapter summarized several optical concepts underlying the optimal coverage problem, including the work in [2], on which the research for this paper is based. Knowledge of this chapters' topics is fundamental in formulating Chapters III and IV.

CHAPTER III

PREVIOUS WORK

The topics discussed in this chapter serve as the foundation for the current research; conclusions reached from [2] will be summarized here for the reader, while a deeper understanding can be obtained from this reference. The equations given in this chapter are integral in understanding Chapters IV and V. For some equations in [2], minor notation changes were made to more closely align with the notation used in the present study. Specifically, subscripts n and k were often rewritten as m and n when two apertures are considered to allow for a better consistency and understanding of the formulae. Also, in [2] the frequency plane is sometimes referred to as the (u, v) plane or the spatial frequency plane. In this paper, the preferred term is the frequency plane to avoid confusion.

A metric was given in [2] that describes image quality for autonomous space-borne imaging systems. First-order necessary conditions were expressed that must be met to achieve the desired quality in the frequency plane. Special cases were then used to analyze the relation between coverage algorithms and the necessary conditions. Note that the optimality conditions of the spacecraft maneuvers were characterized by achieving high quality images.

A. Image Quality Metric

The image quality metric was based on a measure of fuel and time required for the space-borne spacecraft containing the apertures to achieve the desired image quality.

As stated in Chapter II, after the light from the apertures is collected, the image

is obtained by performing the IFT. The bound on the mean square error was then derived based on the MTF at time t and the standard deviation of the noise. The ratio of the magnitude of the MTF to the standard deviation of the noise is essentially the signal-to-noise ratio (SNR). This ratio must be greater than a desired SNR (SNR_d) to meet the performance specifications.

The measure of image quality was defined as Γ and is given in equation (3.1) for $m \neq n$. Γ is measured as the coverage discs sweep through the frequency plane; its value starts at zero for the initial image acquisition time and accumulates to a value of unity. Achieving values of Γ very close to one indicates that the image will have a desirable quality and allows for reconstruction of the image. An acceptable image is obtained for SNR_d and resolution when $\Gamma \approx 1$ within the entire resolution disc.

$$\Gamma(\vec{u},t) \triangleq \frac{\kappa - \frac{4\mu}{\kappa\eta^2}}{SNR_d(\vec{u})}\sqrt{\tilde{M}(\vec{u},t)} \quad \triangleq \int_0^t d\boldsymbol{\tau} \sum_{m,n} \hat{A}_P\left(\vec{u} - \frac{1}{\lambda}\big(\vec{\chi}_m(\boldsymbol{\tau}) - \vec{\chi}_n(\boldsymbol{\tau})\big)\right) \tag{3.1}$$

Γ is a function of the wavelength, λ, the position of the coverage disc in the frequency plane, $\vec{u}$, the aperture positions in the frequency plane, χ_m and χ_n, and

$$\tilde{M}(\vec{u},t) = \int_0^t d\boldsymbol{\tau} \sum_{m=1}^{N}\sum_{n=1}^{N} \Omega_{m,n}\left|\hat{A}_P\left(\vec{u} - \frac{1}{\lambda}\big(\vec{\chi}_m(\boldsymbol{\tau}) - \vec{\chi}_n(\boldsymbol{\tau})\big)\right)\right|^2 \tag{3.2}$$

As a side note, a similar formula for $M(\vec{u},t)$ characterizes the overall OTF of the imaging system:

$$M(\vec{u},t) = \int_0^t d\boldsymbol{\tau} \sum_{m=1}^{N}\sum_{n=1}^{N} \Omega_{m,n}\hat{A}_P\left(\vec{u} - \frac{1}{\lambda}\big(\vec{\chi}_m(\boldsymbol{\tau}) - \vec{\chi}_n(\boldsymbol{\tau})\big)\right) \tag{3.3}$$

Here,

$$\Omega_{m,n} = \begin{cases} 1 & \text{For measurement between apertures } m \text{ and } n \\ 0 & \text{If no measurement is made} \end{cases}$$

The expression for Γ was derived based on SNR_d, the positions of the apertures represented in the frequency plane, χ_m and χ_n and the normalized field-of view function, $\hat{A}_P$, which is defined as

$$\hat{A}_P(\vec{u}) = \frac{\hat{A}_P(\vec{u})}{\hat{A}_P(0)} \tag{3.4}$$

where $\hat{A}_P(\vec{u})$ is the Fourier transform of the picture field-of-view function:

$$A_P(\theta) = \begin{cases} 1 & \text{If } \vec{\theta} \text{ falls within in the desired picture frame} \\ 0 & \text{Otherwise} \end{cases}$$

Also, in equation (3.1),

$$\kappa = \sqrt{\frac{4\mu}{\eta^2} + \hat{I}_{est}} \tag{3.5}$$

for a weight, μ, the quantum efficiency, η, and an average of the intensity between two apertures,

$$\hat{I}_{est} = \frac{1}{2}\big(I_1 + I_2\big) \tag{3.6}$$

B. Coverage Problem

To achieve the desired image quality, the coverage discs must sweep through the entire resolution circle and generate a value of approximately $\Gamma = 1$ for the entire circle interior. The motion of the coverage discs corresponds to the relative positions

of the apertures in the spatial plane. One way to visualize this method is to imagine spraying a can of paint over a circular region with the intention of just saturating the entire area; full saturation must be achieved, while over-saturation is not an efficient use of time or paint. For instance, Figure (9) shows the two coverage discs moving through the resolution plane at a speed that will ensure full coverage within almost all of the coverage discs' paths. A small outer ring about the edge of the coverage discs may achieve partial coverage (i.e., the painted area is not saturated) if a speed resulting in full coverage is not achieved. More discussion about this so-called critical speed will be discussed in Chapter IV. The number of coverage discs seen in the frequency plane is

$$N_C = N(N-1) \tag{3.7}$$

where N is the number of apertures in the entire system. Figure (9) shows the coverage scenario for $N = 2$ apertures, corresponding to $N_C = 1$. However, because of the mirrored nature of the frequency plane, two coverage discs are seen; one is the mirrored image of the other.

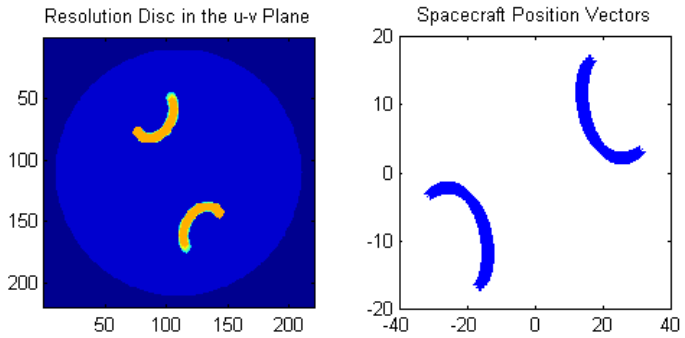

Fig. 9. Coverage discs within the resolution plane (N = 2 apertures)

C. Coverage Algorithms

The coverage problem focuses on optimizing the maneuvers of the spacecraft carrying the separate apertures that will optimize the image quality. Since covering the entire resolution plane using the coverage discs is necessary, an obvious solution would be to increase the number of apertures. However, space-borne telescopes have limitations on size, cost, and deployment strategies. Various coverage strategies may be investigated to determine the optimal method by which the resolution plane may be covered. For instance, the coverage discs could move in a straight line and only turn when reaching the edge of the resolution disc or an area that has already been covered. Another strategy is for the coverage discs to move in a circular motion such that the covered path spirals outward until it reaches one of these same boundaries. Chapter V will give a heuristic comparison of these strategies.

Continuing the paint coverage analogy, Γ may be considered the opacity of the

coat of paint. $\Gamma \leq 1$ signifies partial coverage and an inadequate SNR, while $\Gamma = 1$ means $SNR \geq SNR_d$ and ensures full coverage of the coverage disc's path in the resolution disc. The thickness of the coat of paint is determined by the amount of time a coverage disc spends at any part of the resolution disc and is quantified by equation (3.8). Its value starts at zero at the beginning of the imaging process and is defined as

$$z(\vec{u}, t) = \int_0^t d\tau \sum_{m,n} \hat{A}_P\big(\vec{u} - \vec{\chi}_{mn}(\tau)\big) \tag{3.8}$$

where $\hat{A}_P$ has a value of unity for position vectors within the resolution disc:

$$\hat{A}_P(\vec{u}) = \begin{cases} 1 & \text{if } |\vec{u}| \leq r_{D_R} \\ 0 & \text{if } |\vec{u}| > r_{D_R} \end{cases}$$

The position of coverage disc mn is given as $\vec{\chi}_{mn}$ in the frequency plane as a function of the spatial plane spacecraft positions $\vec{x}_m(t)$ and $\vec{x}_n(t)$:

$$\vec{\chi}_{mn} = \frac{1}{\lambda}\big(\vec{x}_m(t) - \vec{x}_n(t)\big) \tag{3.9}$$

A saturation function based on each spacecraft location was defined for the spacecraft first order necessary conditions, described in the next section, as

$$H(x) = \begin{cases} x & 0 \leq x \leq 1 \\ 1 & x > 1 \end{cases}$$

The functions describing the opacity and thickness of the hypothetical paint are related through the following equation:

$$\Gamma(\vec{u},t) = H\sqrt{z(\vec{u},t)} \tag{3.10}$$

Taking the derivative of equation (3.10) results in

$$H'(x) = \begin{cases} 1 & 0 \leq x \leq 1 \\ 0 & x > 1 \end{cases}$$

Another definition leading to the description of the motion of the spacecraft is the gradient function, which is a set of delta functions pointing outward from the coverage disc:

$$\vec{G}(\vec{u}) = \nabla_{\vec{u}}\hat{A}_P(\vec{u}) \tag{3.11}$$

D. Necessary Conditions

A summary will now be given for the first-order necessary conditions (FONC) for optimal coverage of the resolution disc.

N free-flying spacecraft, each containing a single aperture, were considered. The inertial position of the k_{th} spacecraft at time t was denoted as $\vec{x}_k(t)$, and the motion of the spacecraft was described for $k = 1, ...N$ using

$$\frac{d}{dt}\vec{x}_k = \dot{\vec{x}}_k = \vec{v}_k \tag{3.12}$$

$$\frac{d}{dt}\vec{v}_k = \dot{\vec{v}}_k = \ddot{\vec{x}}_k = \vec{T}_k \tag{3.13}$$

where $\vec{x}_k$ is the position of the k_{th} spacecraft, $\vec{v}_k$ is the velocity of the k_{th} spacecraft, and $\vec{T}_k$ is the control thrust on the k_{th} spacecraft. The initial conditions are defined

as

$$\vec{x}_k(0) = x_{k0} \tag{3.14}$$

$$\dot{\vec{x}}_k(0) = v_{k0} \tag{3.15}$$

Next, the expression for Γ in equation (3.1) was set as the image quality penalty, and the cost function was then defined over the resolution disc, D_R, in the frequency domain, $\vec{u}$, over a given time period. The cost is based on a squared weighted norm of the control force and a measure of frequency plane coverage. The cost function, given in equation (3.16), depends on the control thrust, the image quality metric Γ having values from zero to unity, variable weighting factor μ, discount factor T_h, and partial coverage exponent R. Smaller values of R encourage partial coverage, while smaller values of T_h place more emphasis on near future events. The ultimate goal of future studies is to determine an optimal control law for simple cases where T_h is small, and then to expand those laws to include a larger time horizon.

$$J = \int_0^\infty e^{-t/T_h} \left[\int_0^{D_R} d\vec{u} \left[1 - H\left(\Gamma^R(\vec{u}, t) \right) \right] + \mu \sum_{k=1}^{N} \left| \vec{T}_k \right|^2 \right] dt \tag{3.16}$$

After completing detailed steps of the derivation, the FONC were summarized as follows for $k = 1, ..., N$ and $m \neq n$:

$$\ddot{\vec{x}}_k = \vec{T}_k \tag{3.17}$$

$$\vec{x}_k(0) = \vec{x}_{k0} \tag{3.18}$$

$$\dot{\vec{x}}_k(0) = \dot{\vec{x}}_{k0} \tag{3.19}$$

$$e^{t/T_h}\frac{d^2}{dt^2}\big(e^{-t/T_h}\vec{T}_k\big) = \tag{3.20}$$
$$-\frac{R}{2\mu}\sum_{m\neq n}\int_t^\infty d\tau e^{-(\tau-t)/T_h}\int_0^{D_R} d\vec{u}H'\big(\Gamma(\vec{u},\tau)\big)\Gamma^{R-1}(\vec{u},\tau)\left[\vec{G}\left(\vec{u}-\vec{\chi}_{mn}(t)\right)-\vec{G}\left(\vec{u}-\vec{\chi}_{mn}(t)\right)\right]$$

where

$$H\big(\Gamma(\vec{u},t)\big) = \begin{cases}\Gamma(\vec{u},t) & \text{if } \left|\Gamma(\vec{u},t)\right| \leq 1 \\ 1 & \text{if } \left|\Gamma(\vec{u},t)\right| > 1\end{cases} \tag{3.21}$$

$$\vec{G}(\vec{u}) \triangleq \nabla_{\vec{u}}\hat{A}_P(\vec{u}) \tag{3.22}$$

$$\lim_{t\to\infty}\left[e^{-t/T_h}\vec{T}_k\right] = 0 \tag{3.23}$$

$$\lim_{t\to\infty}\left[\frac{d}{dt}\big(e^{-t/T_h}\vec{T}_k\big)\right] = 0 \tag{3.24}$$

$$\Gamma(\vec{u},t) \triangleq \int_0^t d\tau\sum_{m,n}\hat{A}_P\big(\vec{u}-\vec{\chi}_{mn}(\tau)\big) \tag{3.25}$$

$$\vec{\chi}_{mn}(t) \triangleq \frac{1}{\lambda}\left(\vec{x}_m(t)-\vec{x}_n(t)\right) \tag{3.26}$$

Chapter V of [2] provides more information on general coverage disc motion. To obtain insight into general motion strategies, simplified cases were studied.

E. Special Cases of the Necessary Conditions

Special cases of the FONC relevant to imaging with multiple spacecraft were then considered, leading to simplifications of the necessary conditions. The cases considered

include

1. Large Resolution Disc and Limited Time Horizon Approximations
2. One-Dimensional Motion Approximations
3. Lower Bound on Imaging Time for Single Pass Coverage

Using the special cases, several simplifications were made. When the resolution disc is much larger than the coverage disc, the time horizon parameter is extremely small when compared with the time necessary for full coverage of the entire resolution disc and the control force can be simplified. For one-dimensional motion of a single coverage disc, the speed is on the order of two times the radius of the resolution disc, so

$$\frac{R}{\mu}\left(\frac{1}{T_h}\right)^2 << 1 \tag{3.27}$$

Lastly, a lower bound for the minimum imaging time was found.

The motion of free-flying spacecraft along one dimension may be summarized as follows, given the preceding definitions. These conditions describe a pseudo-force, or difference in control thrust between m and n spacecraft, as seen in the frequency plane for $m, n = 1, ..., N$, where τ is some general time in the future:

$$\ddot{\vec{\chi}}_{mn} = \vec{F}_{mn}(t) \tag{3.28}$$

$$\vec{F}_{mn}(t) = -\frac{2R}{\mu}\int_t^\infty dt_2 \int_{t_2}^\infty dt_1 e^{-(t_1-t)/T_h}\vec{f}_{mn}(t_1) \tag{3.29}$$

$$\vec{f}_{mn}(t_1) = \int_{t_1}^{\infty} d\tau e^{-(\tau - t_1)/T_h} \int_0^{D_R} d\vec{u} H'\big(\Gamma(\vec{u},\tau)\big)\Gamma^{R-1}(\vec{u},\tau)\Big[\vec{G}\big(\vec{u}-\vec{\chi}_{mn}(t_1)\big)-\vec{\Psi}_{mk}(\vec{u},t_1)\Big] \tag{3.30}$$

$$\vec{\Psi}_{mk}(\vec{u},t) \triangleq \frac{1}{2}\sum_{n\neq m,k}\Big[\vec{G}\big(\vec{u}-\vec{\chi}_{nm}(t)\big)+\vec{G}\big(\vec{u}-\vec{\chi}_{kn}(t)\big)\Big] \tag{3.31}$$

$$\Gamma(\vec{u},t) \triangleq \int_0^t d\tau \sum_{m,n}\hat{A}_P\big(\vec{u}-\vec{\chi}_{mn}(\tau)\big) \tag{3.32}$$

This study focused on simulations using $N = 2$ apertures, in which case $\vec{\Psi}_{mn}(\vec{u},t_1) = 0$. Using these assumptions and simplifications, the results on pages 107-108 of [2] will be compared with the results of the present study in Chapters IV and V.

F. Summary

This chapter summarized the work of [2], upon which the current study was built. A paint metaphor was given to help visualize the optimal painting strategy and corresponding parameters and requirements. The cost function and first-order necessary conditions were presented and will be used throughout the rest of this paper. The paint coverage metaphor will be revisited in Chapter IV as a thin-paintbrush analogy to approximate the instantaneous velocity of a coverage disc. Also, in Chapters IV and V, the current work investigates the special case of rectilinear motion for a relatively large resolution disc and limited time horizon parameter.

CHAPTER IV

PROBLEM FORMULATION

The previous work in [2] assumed constant motion of the aperture-carrying spacecraft for all time, including that for $t = 0$, which provided insightful results. The following derivation builds upon this previous work through the addition of an initial stationary state of motion. Specifically, the coverage disc is assumed to be initially stationary. This disc will be shown to be unstable and that one solution of the FONC for the subsequent motion is rectilinear travel with time-varying acceleration to reach a constant, terminal velocity. In future work, analyses may build upon such simplified cases to gain a better understanding of optimized general motion.

A. Derivation of Time-Dependent Velocity Equations

Figure (10) shows one coverage disc at $t = 0$, where the center of the disc is located at the origin of the given coordinate system. For now, the origin shall remain fixed at the initial coverage disc center, while the coverage disc moves linearly along the $+x$ axis. Recall that this coverage disc will be mirrored in the frequency plane such that two discs would appear in any simulation.

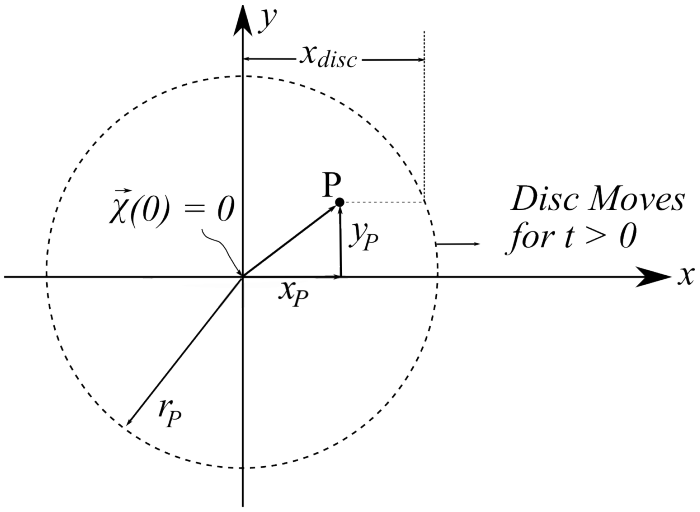

Fig. 10. Resolution disc at t = 0

The general equations representing the pseudo-force are determined by simplifying the FONC in equations (3.28) - (3.32). Here, Γ is a function of only one aperture function, so the summation in equation (3.25) is unnecessary. Also, the subscripts m and n are not included since only two apertures are considered, and the $\int_{D_R} d\vec{u}$ term indicates an integral over the two-dimensional frequency plane. The expression for the pseudo-force in this case is

$$\ddot{\chi} = \vec{F}(t) \tag{4.1}$$

$$\vec{F}(t) = -\frac{2RT_h^2}{\mu} \int_t^{\infty} d\tau \, e^{-(\tau - t)/T_h} \int_{D_R} du \; H'\big(\Gamma(\vec{u}, \tau)\big) \Gamma^{R-1}(\vec{u}, \tau) \vec{G}\big(\vec{u} - \chi(t)\big) \tag{4.2}$$

$$\Gamma(\vec{u}, \tau) = \int_0^{\tau} d\tau \, \hat{A}_P\big(\vec{u} - \chi(\tau)\big) \tag{4.3}$$

$$\vec{G}(\vec{u}) = \nabla_{\vec{u}} \hat{A}_P(\vec{u}) \tag{4.4}$$

A simplification to one-dimensional motion along the $\hat{x}$ direction simplifies these equations to

$$\ddot{\chi} = F(t) \tag{4.5}$$

$$F(t) = \frac{-2RT_h^2}{\mu} \int_t^\infty d\tau \, e^{-(\tau - t)/T_h} \int_{D_R} du \, H'\big(\Gamma(\vec{u}, \tau)\big) \Gamma^{R-1}(\vec{u}, \tau) G\big(\vec{u} - \chi(t) \cdot \hat{x}\big) \tag{4.6}$$

$$\Gamma(\vec{u}, \tau) = \int_0^\tau d\tau \, \hat{A}_P\big(\vec{u} - \chi(\tau)\hat{x}\big) \tag{4.7}$$

$$G(\vec{u}) = \hat{x} \cdot \nabla_{\vec{u}} \hat{A}_P(\vec{u}), \tag{4.8}$$

where the only difference from equations (4.1) - (4.4) is the inclusion of the $\hat{x}$ term. In equation (4.6), note that

$$H'\big(\Gamma(\vec{u}, \tau)\big) \Gamma^{R-1}(\vec{u}, \tau) = \begin{cases} \Gamma^{R-1}(\vec{u}, \tau); & \Gamma(\vec{u}, \tau) \leq 1 \\ 0; & \Gamma(\vec{u}, \tau) > 1 \end{cases} \tag{4.9}$$

which may be substituted directly back into the equation:

$$F(t) = -\frac{2RT_h^2}{\mu} \int_t^\infty d\tau \, e^{-(\tau - t)/T_h} \int_{D_R} du \, G\Big(\vec{u} - \chi(t) \cdot \hat{x}\Big) \begin{cases} \Gamma^{R-1}(\vec{u}, \tau); & \Gamma(\vec{u}, \tau) \leq 1 \\ 0; & \Gamma(\vec{u}, \tau) > 1 \end{cases} \tag{4.10}$$

Next, a new variable of integration is defined to be $\vec{u}' = \vec{u} - \hat{x} \cdot \chi(t)$ such that the origin is always at the center of the disc as it translates. The equation for the pseudo-force may be represented in terms of $\vec{u}'$ as

$$F(t) = -\frac{2RT_h^2}{\mu}\int_t^\infty d\tau\, e^{-(\tau-t)/T_h}\int_{D_R} du'\, G(\vec{u}')\begin{cases}\Gamma^{R-1}\Big(\vec{u}'+\hat{x}\cdot\chi(t),\tau\Big); & \Gamma(\vec{u},\tau)\le 1\\ 0; & \Gamma(\vec{u},\tau)>1\end{cases} \tag{4.11}$$

where

$$G(\vec{u}') = G(\vec{u}-\vec{\chi}(t)\cdot\hat{x}) \tag{4.12}$$

Let $\vec{u}' = r_P cos(\theta)\hat{x} + r_P sin(\theta)\hat{y}$ and define

$$B(\tau,t) = -\int_{D_R} du'\,\vec{G}(\vec{u}')\begin{cases}\Gamma^{R-1}\Big(\vec{u}'+\hat{x}\cdot\chi(t),\tau\Big); & \Gamma\big(\vec{u}'+\hat{x}\cdot\chi(t),\tau\big)\le 1\\ 0; & \Gamma\big(\vec{u}'+\hat{x}\cdot\chi(t),\tau\big)>1\end{cases} \tag{4.13}$$

Equation (4.11) may be converted to polar coordinates in the $\vec{u}'$ plane, where the y coordinates cancel due to symmetry, using the gradient function that consists of delta functions:

$$G(\vec{u}) = -\delta(r-r_P)\big[\hat{x}cos(\theta)+\hat{y}sin(\theta)\big]\cdot\hat{x} \tag{4.14}$$

$$= -\delta(r-r_P)cos(\theta) \tag{4.15}$$

and

$$\Gamma(\vec{u}'+\hat{x}\cdot\chi(t),\tau) = \int_0^t d\tau\,\hat{A}_P\big(\vec{u}'+\hat{x}\cdot\big(\chi(t)-\chi(\tau)\big)\big) \tag{4.16}$$

Using polar coordinates results in an expression for the pseudo-force dependent upon a time-varying velocity,

$$F(t) = \frac{2RT_h^2}{\mu} \int_t^\infty d\tau \, e^{-(\tau - t)/T_h} B(\tau, t) \tag{4.17}$$

where B is simplified using the sifting property on $\vec{G}$:

$$B(\tau, t) = 2r_P \int_0^\pi cos\theta d\theta \begin{cases} \Gamma^{R-1}\Big(\vec{u}' + \hat{x} \cdot \chi(t), \tau\Big); & \Gamma(\vec{u}' + \hat{x} \cdot \chi(t), \tau) \leq 1 \\ 0; & \Gamma(\vec{u}' + \hat{x} \cdot \chi(t), \tau) > 1 \end{cases} \tag{4.18}$$

and leads to a simplified equation for Γ using equation (2.23):

$$\Gamma(\vec{u}' + \hat{x} \cdot \chi(t), \tau) = \int_0^\tau d\tau \begin{cases} 1; & \sqrt{\big(r_P cos\theta + \chi(t) - \chi(\tau)\big)^2 + r_P^2 sin^2\theta} \leq r_P \\ 0; & \text{Otherwise} \end{cases} \tag{4.19}$$

Recall that $\vec{u}' = r_P cos\theta \hat{x} + r_P sin\theta \hat{y}$.

When the weighting factor μ is large, the pseudo-force must be very small, and χ varies only gradually. The force integrals depend on a time interval $\tau - t$, rather than explicitly on either τ or t, while the force itself depends upon the velocity at the current time. When the accelerations of the coverage discs are very small, the duration required for the disc to move one diameter may be determined. During this time period, if $\dot{\chi}$ varies slowly, it can be approximated as a constant value for a future time interval. Then $\chi = \int \dot{\chi}$ is a locally, linearly, time-varying quantity. Note that the main focus is on $\chi(\tau - t)$, not on the absolute value of χ at any instant in time, and depends on the future rate $\dot{\chi}$. Assuming a constant value of the speed of the coverage disc leads to a simplified version of the equations of motion.

B. Thin Paintbrush Metaphor

Previously the concept of a paintbrush was used to describe the effectiveness of spatial frequency plane coverage as related to the desired SNR. This idea is expanded further to explain the coverage behavior for velocities approaching zero.

For the proposed thin paintbrush hypothesis, the brush crosses a point in the resolution disc almost instantaneously. Therefore, $\chi(t)$ may be replaced with with $\ddot{\vec{\chi}}t$, which is a constant value, for the current generalized narrow time range $t \in [0, \infty)$. As will be shown, the velocity of the coverage disc may be approximated while a given point is within that disc.

1. Review of FONC

An approximation for the FONC will be discussed that leads to reduced equations for easy implementation.

For $N = 2$, the first order necessary conditions are rewritten from equations (3.17) - (3.26) as

$$\ddot{\vec{\chi}} = \vec{F}(t) \tag{4.20}$$

$$\begin{aligned} \vec{\chi}(0) &= 0 \\ \dot{\vec{\chi}}(0) &= 0 \end{aligned} \tag{4.21}$$

$$\ddot{\vec{F}} - \frac{2}{T_h}\dot{\vec{F}} + \frac{1}{T_h^2}\vec{F} \tag{4.22}$$

$$= -\frac{2R}{\mu}\int_t^\infty d\tau e^{-(\tau-t)T_h}\int_{D_R} duH'\big(\Gamma(\vec{u},\tau)\big)\Gamma^{R-1}(\vec{u},\tau)G\big(\vec{u}-\vec{\chi}(t)\big) \tag{4.23}$$

Next, define an un-weighted pseudo-force:

$$\vec{f}(t) = -\int_t^\infty d\tau e^{-(\tau-t)T_h}\int_{D_R} duH'\big(\Gamma(\vec{u},\tau)\big)\Gamma^{R-1}(\vec{u},\tau)G\big(\vec{u}-\vec{\chi}(t)\big) \tag{4.24}$$

where $\vec{f}(t)$ depends on $\vec{v}(t) = \dot{\vec{\chi}}(t)$. Also,

$$\lim_{t\to\infty}\left[e^{-t/T_h}\vec{F}(t)\right] = \lim_{t\to\infty}\left[\frac{d}{dt}\Big(e^{-t/T_h}\vec{F}(t)\Big)\right] = 0 \tag{4.25}$$

Γ depends on the entire time history of χ. Since Γ is a function of χ, the integrand in equation (4.24) is nonzero when $\chi(t)$ is within the coverage disc. Note that the integrals in equation (4.24) depend upon finite intervals, not the entire time history; the equation is written as a generalization. In order to satisfy the final condition, the initial conditions in equation (4.21) plus initial conditions on $\vec{F}$ and $\dot{\vec{F}}$ must be satisfied. Therefore, if these conditions are followed, the steady state condition of the coverage disc results in a correct solution to the FONC. In order to solve the two-point boundary problem, an integration method is required, and the following approximation is used to obtain the solution.

2. Law of the Mean

A velocity approximataion, described in the next section, uses the Law of the Mean over a given time period. Implementing this theorem is critical in obtaining an accurate velocity approximation. Let the function $g(t)$ be continuous and differentiable

over the interval $[a, b]$. Let $\varepsilon, \xi \in [a, b]$ such that

$$g(b) - g(a) = \left(\frac{dg}{dt}\right)_c (b - a). \tag{4.26}$$

At least one point along g, defined generally here as c, has a first derivative that is parallel to the secant joining a and b. In this manner, a slope can always be found that matches the slope of the secant; see Figure (11) for an example. The use of this theorem is critical in obtaining a velocity approximation over a given time period.

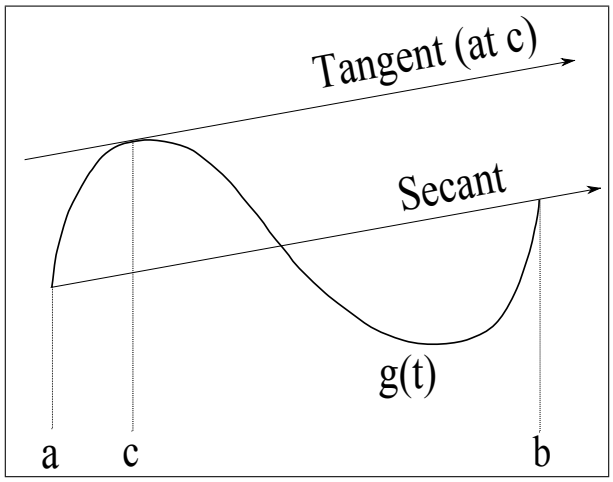

Fig. 11. Mean value theorem

3. Velocity Approximation

For now, let χ be the instantaneous center of the coverage disc. Observe the following coverage disc scenario in Figure (12). x_P is the location at which the point under consideration lies just within the interior of the coverage disc; similarly, $t(\chi_P)$ is the time at which this point enters the interior of the disc. The time during which the point lies within the moving disc may be calculated:

$$t_{disc} = t\Big(\chi + \sqrt{r_P^2 - y_P^2}\Big) - t\Big(\chi - \sqrt{r_P^2 - y_P^2}\Big) \tag{4.27}$$

$$= t(\chi_P) - t\Big(\chi - \sqrt{r_P^2 - y_P^2}\Big) \tag{4.28}$$

for

$$x_P \leq \chi - \sqrt{r_P^2 - y_P^2} \tag{4.29}$$

Here, constant velocity is not assumed, and t is not a linear function of χ; note that this expands upon the previous work of [2].

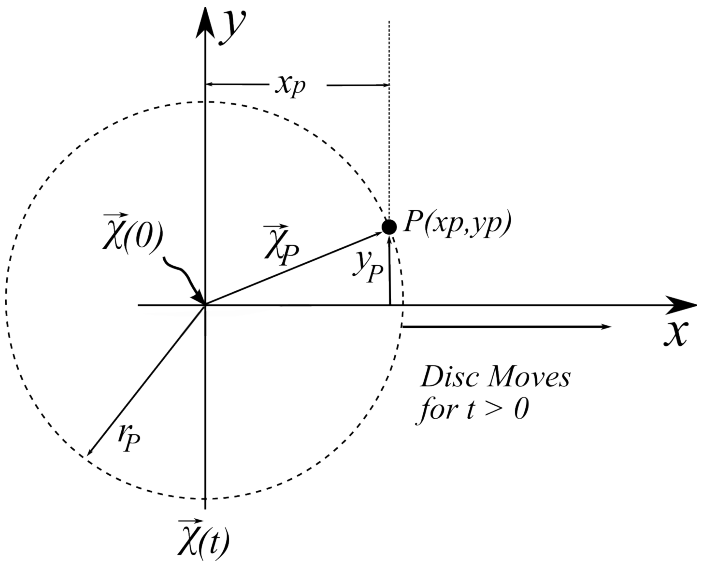

Fig. 12. Coverage disc for thin paintbrush analogy

Γ has one of two values, based on the location of the point under consideration; if the point is not within the coverage disc, Γ has a value of zero. If the point lies within the disc, Γ has a value determined by the location of the point. These two possible values are summarized as follows:

$$\Gamma(x_P, y_P) = \begin{cases} 0; & x_P > \sqrt{r_P^2 - y_P^2} + \chi \\ t(\chi_P) - t\big(\sqrt{r_P^2 - y_P^2} + \chi\big); & \chi - \sqrt{r_P^2 - y_P^2} \leq \chi_P \leq \sqrt{r_P^2 - y_P^2} + \chi \end{cases} \tag{4.30}$$

The calculation for Γ depends upon the time a point spends within the interior of the coverage plane, which in turn is based upon the velocity of the coverage disc during the corresponding time period. Knowledge of $t(\chi_P)$ may be be used to approximate the velocity of the disc while a point lies within its interior using the Law of the Mean as follows. A thin paintbrush approximation is made when $\chi(t)$ is assumed to be at the center of the disc; the instantaneous velocity of the entire coverage disc is considered constant. Similarly, a thin paintbrush would move over an area with a constant speed throughout at any given instant. It is important to note that this velocity is not constant over the entire time interval. Then the difference between 1) the time a given point enters the interior of the resolution disc and 2) the time that same point exits the interior of the moving resolution disc is calculated using the typical formula for a constant velocity. Here, the change in time may be written using equation (4.32), where $\tilde{\chi}$ is a point somewhere in the middle of the considered point's linear path and $\tilde{\chi}$ lies within the resolution disc at t.

$$t(\chi_P) - t\big(\sqrt{r_P^2 - y_P^2} + \chi\big) = \frac{dt(\tilde{\chi})}{d\chi}\left(\chi_P - \chi - \sqrt{r_P^2 - y_P^2}\right) \tag{4.31}$$

$$\frac{dt(\tilde{\chi})}{d\chi} = \frac{1}{\frac{d\chi}{dt}} \tag{4.32}$$

The approximation given in this section is anticipated to hold true for large values of acceleration. Because

$$\vec{v} = \dot{\vec{\chi}} \tag{4.33}$$

and

$$\dot{\vec{v}} = \vec{F} \tag{4.34}$$

then

$$\dot{\vec{v}} = \ddot{\vec{\chi}} \tag{4.35}$$

Equation (3.20) expresses the adjoint equation as

$$\ddot{\vec{F}} - \frac{2}{T_h}\dot{\vec{F}} + \frac{1}{T_h^2}\vec{F} = \frac{2R}{\mu}\vec{f}\big(v(t)\big) \tag{4.36}$$

where $\vec{f}$ is defined in equation (4.24) and $v(0) = 0$ is assumed. As $t \to \infty$,

$$e^{-t/T_h}\vec{F}(t) \to 0 \tag{4.37}$$

$$\frac{d}{dt}\left(e^{-t/T_h}\vec{F}(t)\right) \to 0 \tag{4.38}$$

Figure (13) demonstrates the physical interpretation of the thin paintbrush analogy in the spatial frequency plane. When $\Gamma = 1$, $H = 0$ and the moving coverage disc appears to have a solid outline; its interior is "hollow" for motion at the critical speed, v_c. The grayed regions emphasize those which are partially covered, while the interior is fully covered and has a value of $\Gamma = 1$. When $t \approx 0$, the speed of the coverage disc is less than the critical speed and the solid outline indicating partial coverage is less dominant.

Fig. 13. Coverage disc at critical speed (left) and speed for t $\approx$ 0 (right)

In summary, the thin paintbrush approximation leads to the following reduced equations:

$$\dot{\vec{v}} = \vec{F} \tag{4.39}$$

$$\ddot{\vec{F}} - \frac{2}{T_h}\dot{\vec{F}} + \frac{1}{T_h^2}\vec{F} \tag{4.40}$$

$$= \frac{2R}{\mu}\vec{f}\Big(v(t)\Big) \tag{4.41}$$

These equations may be integrated forward in time, and the force may be plotted as a function of coverage disc speed. The thin paintbrush analogy provides a good approximation to the velocity, resulting in accurate results for the pseudo-force.

4. Using Thin Paintbrush Analogy to Compare with Previous Work

The results found using the thin paintbrush analogy were compared with the previous work in [2]. Figure (14) shows the control force as a function of the speed; this figure matches closely with that of page 108 of [2].

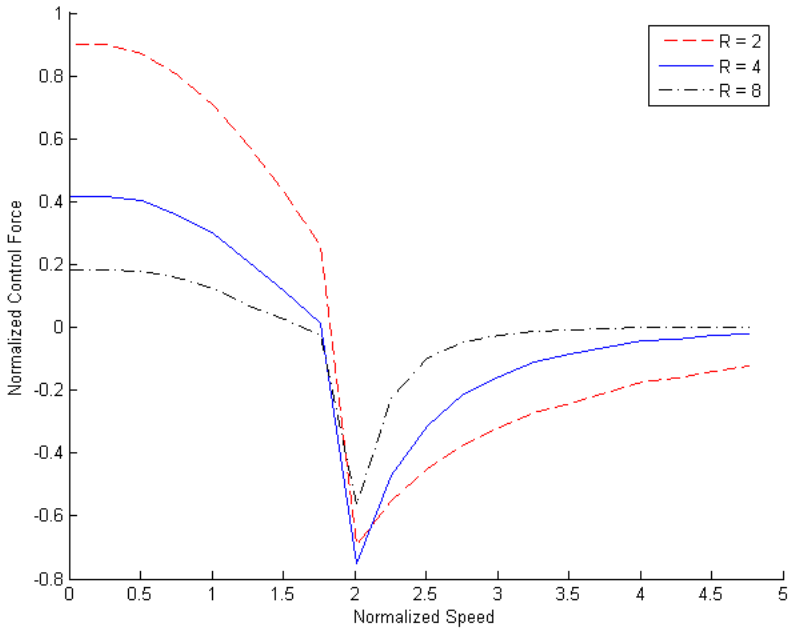

Fig. 14. Coverage disc in motion at critical speed

To focus on a normalized speed less than or equal to the critical speed, which means the disc is accelerating toward the critical speed, the time horizon T_h must be much greater than the time of variation of $\vec{F}$. Here, the curve for $f(v)$ may be approximated as

$$\vec{f}(v) \approx \frac{2}{R}\left(1 - \left(\frac{v}{v_c}\right)^2\right) \tag{4.42}$$

which results in $v_c \approx 5/3$. Also, for speeds less than or equal to the critical speed,

$$\frac{2}{T_h}\dot{\vec{F}} \approx 0 \tag{4.43}$$

$$\frac{1}{T_h^2} \approx 0 \tag{4.44}$$

for

$$x_p \leq \chi(0) - \sqrt{r_p^2 - y_p^2} \tag{4.45}$$

The time during which $\vec{F}$ varies considerably is short. The following derivation shows this proof. First, substitute $\dot{\vec{v}}$ for $\vec{F}$ in equations (4.41) and (4.42). Then the third derivative of the velocity may be rewritten as

$$\frac{d^3\vec{v}}{dt^3} = \frac{4}{\mu}\left(1 + \frac{\vec{v}}{\vec{v}_c}\right)\left(1 - \frac{\vec{v}}{\vec{v}_c}\right) \tag{4.46}$$

At $\vec{v}(0) = 0$, $t \to \infty$ and $\dot{\vec{v}}, \ddot{\vec{v}} \to 0$ because v is constant. Next, let a deviation from $\vec{v}_c$ be defined as $\tilde{v} = \vec{v} - \vec{v}_c$. Substituting $\vec{v} = \tilde{v} + \vec{v}_c$ into equation (4.46) and simplifying yields

$$\frac{d^3\vec{v}}{dt^3} = \frac{4}{\mu}\left(2 + \frac{\tilde{v}}{\vec{v}_c}\right)\frac{1}{\vec{v}_c}\tilde{v} \tag{4.47}$$

If $\vec{v} = 0$,$\tilde{v} = -\vec{v}_c$ for $t \to \infty$ and $\dot{\tilde{v}}, \ddot{\tilde{v}} \to 0$.

Equation (4.47) must be solved approximately and linearized to find a correct solution. At the end of the equation's evolution, $\vec{F}$ should tend toward zero as t approaches positive infinity. Therefore, $\vec{f}(v) \to 0$ as $t \to \infty$, which implies that $\tilde{v} \to 0$ as $t \to \infty$. For large t,

$$\frac{d^3\vec{v}}{dt^3} \approx \frac{8}{\mu}\frac{1}{\vec{v}_c}\tilde{v} \tag{4.48}$$

Again, the terminal conditions must be satisfied for a complete solution for any t to be obtained.

C. Summary

This chapter gave derivations for the time-dependent velocity equations for an initial velocity of zero. It also discussed a velocity approximation and gave a thin paintbrush metaphor to aid in visualizing this approach. The thin paintbrush analogy results showed that the analytical solution found in [2] is an incomplete solution as it does not account for varying velocities of the coverage discs; the reproduced results are shown in Figure (14). This prior analysis relies on the fact that during one time unit, the coverage disc moves one diameter. Correspondingly, the coverage disc must be moving at the critical speed.

CHAPTER V

SIMULATION AND RESULTS

This chapter describes in detail the Matlab simulations used to obtain results verifying the problem formulation. First, a projection will be derived that ensures the coverage disc accelerations meet the control force constraints. Next, the two-point boundary problem for the FONC is solved, and a linearized version of the equations is also solved and compared with the nonlinear equations. After that, the conditions for optimal overlap will be described. Finally, a heuristic comparison between coverage strategies will be presented.

A. Simulation Development

1. Derivation of Projections from Spacecraft Positions to Coverage Areas in the Frequency Plane

The following derivation was necessary for simulation purposes; as will be shown, accelerations may be projected onto a subspace that always meets the imposed control force constraints such that the center of mass is in the system's center. Quality imaging stems from adequate coverage of the spatial frequency plane using N apertures. As a result, this study focuses on the locations of the coverage discs in this plane, leading to a derivation of the corresponding required spacecraft positions. The $N(N-1)$ total coverage discs correspond to half that number of independent coverage discs. The center location of each coverage disc mn in the frequency plane can be represented with spacecraft position vectors $\vec{x}_i$ in the spatial plane as

$$\vec{\chi}_{mn}(t) = \frac{1}{\lambda}\left(\vec{x}_m(t) - \vec{x}_n(t)\right) \tag{5.1}$$

The center positions of the relative position vectors can be explicitly represented as follows [2]:

$$\left[\vec{X}_i\right] \triangleq \begin{pmatrix} \vec{X}_1 \\ \vec{X}_2 \\ \vec{X}_3 \\ \vdots \\ \vec{X}_{N-1} \\ \vec{X}_N \\ \vec{X}_{N+1} \\ \vec{X}_{N+2} \\ \vdots \\ \vec{X}_{2N-1} \\ \vec{X}_{2N-2} \\ \vec{X}_{2N-3} \\ \vec{X}_{2N-4} \\ \vdots \\ \vec{X}_{N(N-1)} \end{pmatrix} = \begin{pmatrix} \vec{\chi}_{12} \\ \vec{\chi}_{13} \\ \vec{\chi}_{14} \\ \vdots \\ \vec{\chi}_{1N} \\ \vec{\chi}_{21} \\ \vec{\chi}_{23} \\ \vec{\chi}_{24} \\ \vdots \\ \vec{\chi}_{2N} \\ \vec{\chi}_{31} \\ \vec{\chi}_{32} \\ \vec{\chi}_{34} \\ \vdots \\ \vec{\chi}_{N,\,N-1} \end{pmatrix} = \frac{1}{\lambda} \begin{bmatrix} 1 & -1 & 0 & 0 & \dots & 0 \\ 1 & 0 & -1 & 0 & \dots & 0 \\ 1 & 0 & 0 & -1 & \dots & 0 \\ \vdots & \vdots & \vdots & \vdots & \vdots & \vdots \\ 1 & 0 & 0 & 0 & \dots & -1 \\ -1 & 1 & 0 & 0 & \dots & 0 \\ 0 & 1 & -1 & 0 & \dots & 0 \\ 0 & 1 & 0 & -1 & \dots & 0 \\ \vdots & \vdots & \vdots & \vdots & \vdots & \vdots \\ 0 & 1 & 0 & 0 & \dots & -1 \\ -1 & 0 & 1 & 0 & \dots & 0 \\ 0 & -1 & 1 & 0 & \dots & 0 \\ 0 & 0 & 1 & -1 & \dots & 0 \\ \vdots & \vdots & \vdots & \vdots & \vdots & \vdots \\ 0 & 0 & 0 & 0 & \dots & 1 \end{bmatrix} \begin{pmatrix} \vec{x}_1 \\ \vec{x}_2 \\ \vec{x}_3 \\ \vec{x}_4 \\ \vdots \\ \vec{x}_N \end{pmatrix}$$

$$\triangleq T \begin{bmatrix} \vec{x}_i \end{bmatrix} \tag{5.2}$$

To observe an entry relating the center of the coverage disc's location to the two contributing spacecraft, note that the relationship is simply related by a matrix of

scalar elements, T:

$$\vec{\chi} = T\vec{x} \tag{5.3}$$

Since this study focuses on finding the spacecraft positions that result in spatial frequency coverage, it would be advantageous to find a relationship for $\vec{x}$ given $\vec{\chi}$. First, T must be shown to be invertible. An additional requirement is that the center of mass of the entire physical system be located at the origin of the determined coordinates. The derivation for this relationship to ensure that the center of mass is at the origin will now be described.

Let $\tilde{x}$ represent coordinates in an arbitrary reference frame. To make $\tilde{x}$ represent the position of the center of mass at the origin, define x such that this is true:

$$\vec{x} = \tilde{x} - \frac{1}{N}\left(\tilde{x}_1 + \tilde{x}_2 + \ldots + \tilde{x}_N\right) \tag{5.4}$$

Next, define a matrix of all ones:

$$U = [1, 1, \ldots, 1]^T \tag{5.5}$$

Equation (5.4) can be rewritten, where $U^T\tilde{x}$ sums the elements of $\tilde{x}$:

$$\vec{x} = \tilde{x} + \frac{1}{N}UU^T\tilde{x} = [I + \frac{1}{N}UU^T]\tilde{x} \tag{5.6}$$

Next, the properties of the original relationship under consideration, equation (5.3), will be discussed. The vector $\vec{\chi}$ has dimension $N(N-1)$ and $\vec{x}$ has dimension N, while T is $N(N-1)$ x N. The rank of T is

$$R[T] = N - 1 \leq N \tag{5.7}$$

$\vec{\chi}$ is a linear combination of the columns of T multiplied by $\vec{x}$. One and only one element of T exists in the mull space. Specifically,

$$TU = 0 \tag{5.8}$$

Lastly, note that the matrix T essentially shifts $\vec{x}$ to the center of mass at the origin of the specified coordinate system.

The following derivation explores a symmetric projection based on the matrix T. First, multiply both sides of equation (5.3) by T^T:

$$T^T\vec{\chi} = T^T T\vec{x} \tag{5.9}$$

Equation (5.9) extracts the linearly independent equations by eliminating the linearly redundant equations and also provides the same information as $\vec{\chi} = T\vec{x}$. This equation is then rearranged for additional analysis:

$$(T^T T)\vec{x} = T^T\vec{\chi} \tag{5.10}$$

The N x N matrix $T^T T$ has a single element in the null space. The following derivation proves that this matrix is invertible.

From observation, the elements on the diagonals of the $T^T T$ matrices have the value $2(N-1)$, while the other elements have values of -2. In summary, the pattern for the matrix $T^T T$ is

$$T^T T = 2NI - 2UU^T \tag{5.11}$$

where I is the identity matrix. Next, a symmetric projection is defined:

$$\tau = \frac{1}{2N}(T^T T) = I - \frac{2}{2N}UU^T = I - \frac{1}{N}UU^T \tag{5.12}$$

The right hand side of this equation is very similar in appearance to that of

equation (5.6). The following proof shows that τ is idempotent; by definition, this means that all powers of itself as well as τ^T are equal to τ. Note that $N = U^T U$.

$$\begin{aligned}
\tau\tau &= (I - \frac{1}{N}UU^T)(I - \frac{1}{N}UU^T) \\
&= I - \frac{1}{N}UU^T - \frac{1}{N}UU^T + \frac{1}{N^2}UU^TUU^T \\
&= I - \frac{2}{N}UU^T + \frac{1}{N}UU^T \\
&= I - \frac{1}{N}UU^T \\
&= \tau
\end{aligned} \tag{5.13}$$

Returning to equation (5.10), first multiply by $\frac{1}{2N}$ on both sides:

$$\frac{1}{2N}(T^T T)x = \frac{1}{2N}T^T\chi \tag{5.14}$$

Next, simplify by using Equation 5.12 and multiply by τ on both sides:

$$\tau\tau x = \frac{1}{(2N)^2}(T^T T)T^T\chi \tag{5.15}$$

Because τ is idempotent, $\tau\tau = \tau$. Then equation (5.15) can be simplified to

$$\tau x = \frac{1}{(2N)^2}(T^T T)T^T\chi \tag{5.16}$$

Equation (5.16) will be revisited for further analysis, but first a short discussion about projections will be given. Any real, symmetric matrix can be written as an eigen expansion:

$$\tau = \Phi\Sigma\Phi^T \tag{5.17}$$

where τ is orthogonal and thus, $\Phi^T = \Phi^{-1}$. Solving for Σ gives

$$\Sigma = \Phi^T \tau \Phi = diag(\sigma_k), \;\; k = 1, \ldots, N \tag{5.18}$$

where σ_k is a diagonal matrix containing the eigenvalues.

Using the fact that τ is idempotent, multiply by Φ^T and Φ (where $\Phi^T\Phi$ gives the identity matrix) on both sides of equation (5.17) to see that

$$\begin{aligned} \tau^2 &= \tau \\ \Phi^T\tau^2\Phi &= \Phi^T\tau\Phi \\ \Phi^T\tau\Phi\Phi^T\tau\Phi &= \Sigma \\ \Sigma^2 &= \Sigma \end{aligned} \tag{5.19}$$

Equation (5.19) shows that for all k, $\sigma_k^2 = \sigma_k$ where $\sigma_k \in \Re$. Also, σ_k has eigenvalues of either 0 or +1. Therefore, τ has one $\sigma_k = 0$ and all other $\sigma_k = 1$. Given an eigenspace

$$\Phi\Sigma\Phi^T v = \Phi \begin{bmatrix} I_{N-1} & 0 \\ 0 & 0 \end{bmatrix} \Phi^T v = \Phi A \Phi^T v \tag{5.20}$$

if the vector on which the operation is performed is three-dimensional, Φv will project that vector onto a plane represented by matrix A. This observation shows that $\Phi^T v$ essentially removes a dimension from the original vector. An $x \in (N-1)$ dimensional subspace can be thought of as being preserved by τ. If τ is applied to x ($\tau x = x$), the original x is returned since it already contains τ.

Returning to equation (5.16) and using $\tau x = x$ gives the resulting equation for x given χ:

$$\vec{x} = \frac{1}{(2N)^2}(T^T T)T^T \vec{\chi} \tag{5.21}$$

Now, suppose that control forces in the simulations do not conform to the constraints. Rather than designing control forces that only meet the designated constraints, these forces may be projected onto a subspace that does meet the constraints. The following example demonstrates this strategy, which is used in the Matlab simulations presented in the next section.

Suppose that $\chi = \tilde{\chi}$ does not meet control force constraints. Only the part of χ that does not meet the constraints must be eliminated. First, write an equation for $\vec{x}$:

$$\vec{x} = \frac{1}{(2N)^2}T(T^T T)T^T \tilde{\chi} \tag{5.22}$$

Equations (5.3) and (5.22) are then used to find a relationship for χ:

$$\begin{aligned} \chi &= Tx \\ &= \frac{1}{(2N)^2}T(T^T T)T^T \tilde{\chi} \end{aligned} \tag{5.23}$$

Next, define a coefficient for χ as

$$\Gamma = \frac{1}{(2N)^2}T(T^T T)T^T \tag{5.24}$$

The following shows that Γ is a projection, using the fact that $T^T T = 2N\tau$ and $\tau^3 = \tau^2 = \tau$:

$$\begin{aligned}
\Gamma^2 &= \frac{1}{(2N)^4} T(T^T T)T^T T(T^T T)T^T \\
&= \frac{1}{(2N)^4} T2N\tau 2N\tau 2N\tau T^T \\
&= \frac{1}{(2N)^2} T\tau^2 2N\tau T^T \\
&= \frac{1}{(2N)^2} T(2N\tau)T^T \\
&= \frac{1}{(2N)^2} T(T^T T)T^T \\
&= \Gamma
\end{aligned} \tag{5.25}$$

Since $\Gamma = (\frac{1}{2N} T^T T)^2$ is a projection, it eliminates portions of $\tilde{\chi}$ that do not obey the control force constraints. Note that $T^T \tilde{\chi}$ is the inner product of the column vectors of T with $\tilde{\chi}$. Also note that the portions of $\tilde{\chi}$ that do not obey the constraints of T are orthogonal to the column vectors.

Lastly, the following derivation shows that $\frac{1}{2N}(TT^T)$ is a projection, leading to a simplified equation for Γ. It is found to be symmetric and positive definite, so all eigenvalues are either zero or positive values. Let

$$\frac{1}{2N} TT^T = \Psi \Lambda \Psi^T \tag{5.26}$$

Equation (5.26) may be manipulated for analysis using $\Lambda = diag(\lambda_k)$, $\lambda_k \in \Re$, $\lambda_k \geq 0$, and $\Psi^T = \Psi^{-1}$:

$$\begin{aligned}
(\frac{1}{2N} TT^T)^2 &= \Psi \Lambda \Psi^T \Psi \Lambda \Psi^T \\
&= \Psi \Lambda I \Lambda \Psi^T \\
&= \Psi (\Lambda)^2 \Psi^T
\end{aligned} \tag{5.27}$$

Here, $(\frac{1}{2N}TT^T)^2$ corresponds to $(\lambda_k)^2 = 0$ or $1 \ \forall \ k$ since it is positive definite. Note that $(\Lambda)^2$ is a diagonal projection. Therefore, equation (5.27) is a projection. In other words, Γ can be simplified to the following equation, which is used during simulations to avoid accelerations that do no obey the control force constraints:

$$\Gamma = \frac{1}{2N}TT^T \tag{5.28}$$

B. Simulation Results

1. Time-Dependent Velocity

As discussed in Chapter IV, the equations governing coverage disc motion were expanded such that the velocity is time-dependent rather than constant for all time. To compare with the previous work of [2], where the velocity was constant, a Matlab simulation solved for the pseudo-force at $R = 2, 4, 6, 8$ for constant velocities. The results closely matched with previous results; see Figure (15) for the simulation results of equation (4.11), where the origin was defined to be at the center of the coverage disc as it moved in a rectilinear fashion.

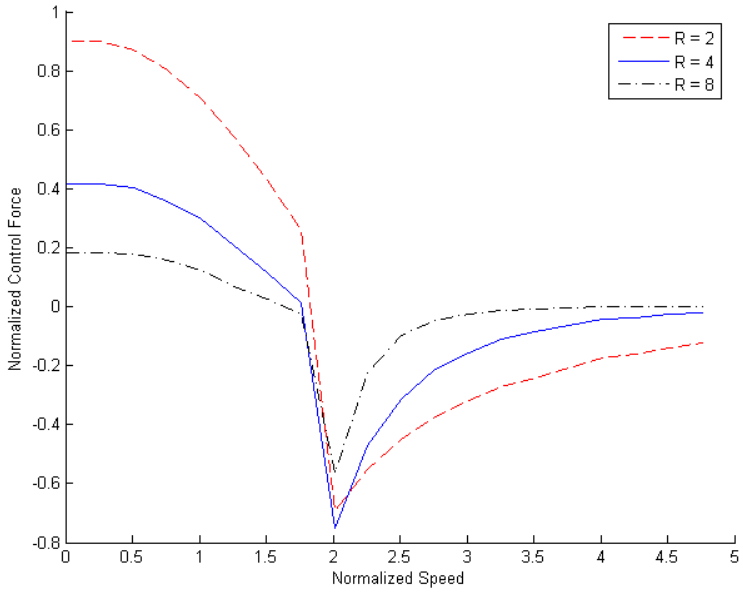

Fig. 15. Simulation of pseudo-force for constant velocities

The critical speed is found where the un-weighted psuedo-force has a zero crossing in Figure (15), which is the speed necessary for full coverage ($\Gamma = 1$) in the first sweep of a coverage disc; it is a stable stationary point. As the risk factor R increases, the initial normalized control force decreases for speeds lower than that of the critical speed. For speeds greater than v_c, higher values of R lead to higher values of the control force. As shown in [2], when $R < 1$, the control force acts to continuously accelerate the coverage disc; it never reaches a desired critical speed. Therefore, only values of $R > 1$ are considered.

2. FONC for One-Dimensional Motion

As seen in Figure (15), the control force is discontinuous. As a result, Newton's Method may not be used to solve the first-order necessary conditions. A linear approximation for the FONC was found to give a result closely matching that of a simplified

expression for the nonlinear FONC. These approximations used simple mathematical equations to represent the unweighted pseudo-force and will be described in the following section.

a. Review of First-Order Necessary Conditions

Recall the analytical approximation for the FONC from equations (4.33) - (4.38), where $v(0)$ is set to zero:

$$\dot{\vec{v}} = \vec{F}$$

$$\ddot{\vec{F}} - \frac{2}{T_h}\dot{\vec{F}} + \frac{1}{T_h^2}\vec{F} = \frac{2R}{\mu}\vec{f}(v) \tag{5.29}$$

$$\lim_{t\to\infty}\left[e^{-t/T_h}\vec{F}(t)\right] \to 0$$

$$\lim_{t\to\infty}\left[\frac{d}{dt}\left(e^{-t/T_h}\vec{F}(t)\right)\right] \to 0 \tag{5.30}$$

Simplifications will now be used for linear and nonlinear representations of $\vec{f}(v)$.

b. Solution Using Approximate $f(v)$

Let $R = 2$, and let the time horizon discount factor, T_h, be a large value such that two terms in the left-hand side of equation (5.29) become negligible. The quantity $\vec{f}(v)$ may be approximated by the equation

$$\vec{f}(v) = \frac{2}{R}\left[1 - \left(\frac{v}{v_c}\right)^2\right] \tag{5.31}$$

$$= \frac{2}{R}\left(1 - \frac{v}{v_c}\right)\left(1 + \frac{v}{v_c}\right) \tag{5.32}$$

Neglecting terms on the order of $\frac{1}{T_h}$, equation (5.29) can be rewritten as

$$\frac{d^3\vec{v}}{d\tilde{t}^3} = \frac{4}{\mu}\left(1 - \frac{\vec{v}}{\vec{v}_c}\right)\left(1 + \frac{\vec{v}}{\vec{v}_c}\right) \tag{5.33}$$

which is exactly the same as equation (4.46). Next, define $\nu = \vec{v}/\vec{v}_c$ and $\tilde{t} = \left(\frac{\mu\vec{v}_c}{8}\right)^{\frac{1}{3}}t$. Then equation (5.33) can simply be expressed as

$$\frac{d^3\vec{v}}{dt^3} = \frac{1}{2}(1+\nu)(1-\nu) \tag{5.34}$$

where

$$\nu(0) = 0 \tag{5.35}$$

$$\lim_{t\to\infty}\left(\frac{d\nu}{dt}\right) = \lim_{t\to\infty}\left(\frac{d^2\nu}{dt^2}\right) = 0 \tag{5.36}$$

To compare the nonlinear solution with the linear solution, rewrite

$$\vec{f} = \frac{2}{R}(1+v')(1-\nu) \tag{5.37}$$

where

$$v' = 1 - \alpha + \alpha\nu \tag{5.38}$$

When $\alpha = 0$, $v' = 1$, and a linear solution is found. Similarly, $\alpha = 1$ gives a nonlinear

solution. Integrating these simple equations forward in time using the Runge-Kutta technique shows that both solutions match very closely with one another. These solutions may also be expressed as powers of the exponential function, as shown in Figures (16) - (18). The best-fit curves E_i for the disc speed, control force, and derivative of the control force with respect to time, respectively, are

$$E_1 = -0.3(0.9e^{-t} + 5e^{-2t} + 2e^{-3t}) + 1.66 \tag{5.39}$$

$$E_2 = 0.8e^{-t} + 1.2e^{-2t} + e^{-3t} \tag{5.40}$$

$$E_3 = -(e^{-t} + 3e^{-2t} + 0.75e^{-3t}) \tag{5.41}$$

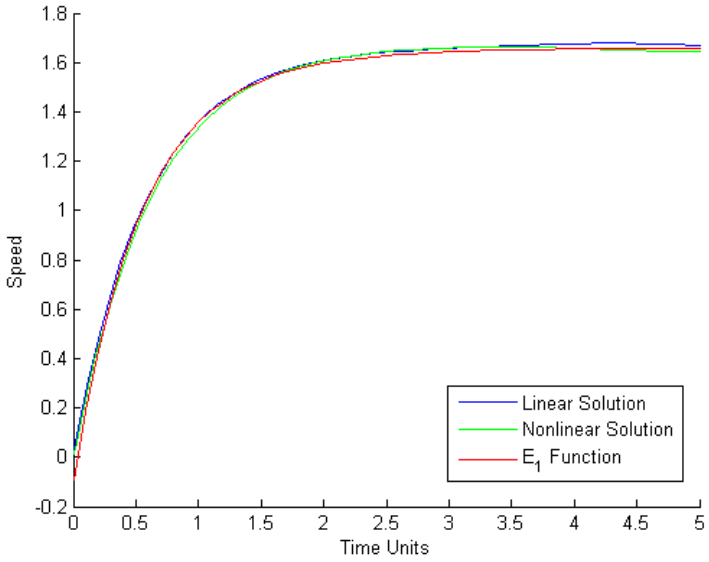

Fig. 16. Comparison of linear and nonlinear solutions to exponential function for disc speed

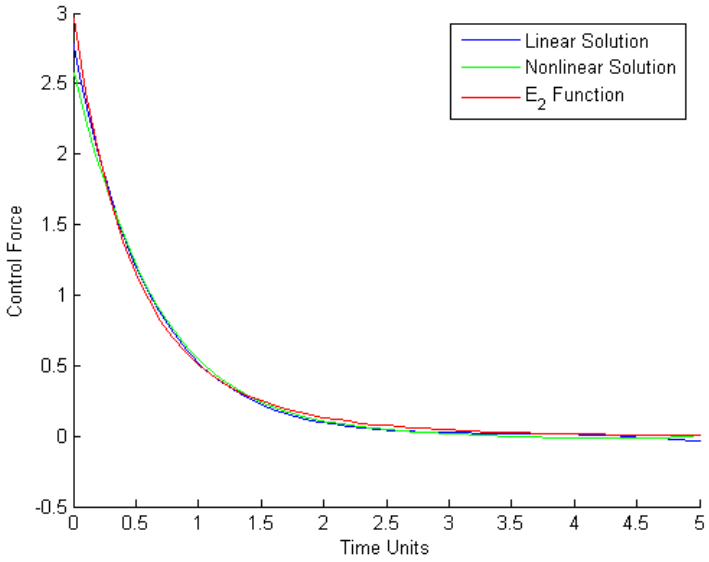

Fig. 17. Comparison of linear and nonlinear solutions to exponential function for control force

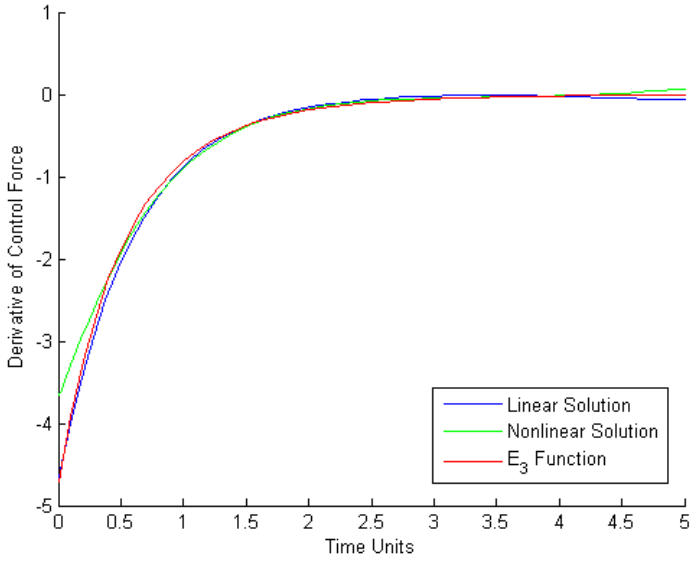

Fig. 18. Comparison of linear and nonlinear solutions to exponential function for derivative of control force

From these plots, it is obvious that the linear, nonlinear, and exponential curves

match closely for the time given and are simply exponential curves. Therefore, a simple control law could be easily be implemented. The disc speed approaches the estimated critical speed, while the control force and derivative of the control force approach zero as expected.

c. Solution Using Best-Fit for Expression of $f(v)$

Next, the approximation for $f(v)$ is shown to be a good approximation when compared with a curve fit to the control force shown in Figure (15). The curve is represented as a polynomial using a best-fit tool in Matlab. The equation that represents $f(v)$ for disc speeds less than the critical speed is given in terms of a high-order polynomial:

$$f(v) = p_1 v^8 + p_2 v^7 + p_3 v^6 + p_4 v^5 + p_5 v^4 + p_6 v^3 + p_7 v^2 + p_8 v + p_9 \tag{5.42}$$

$$p_1 = -2.3681e^{-013}$$

$$p_2 = 1.74e^{-012}$$

$$p_3 = -1.159$$

$$p_4 = 6.0026$$

$$p_5 = -11.624$$

$$p_6 = 10.379$$

$$p_7 = -4.4603$$

$$p_8 = 0.68415$$

$$p_9 = 0.89166$$

This best-fit curve matches closely with the left hand side of the curve showing f vs. v, as shown in Figure (19).

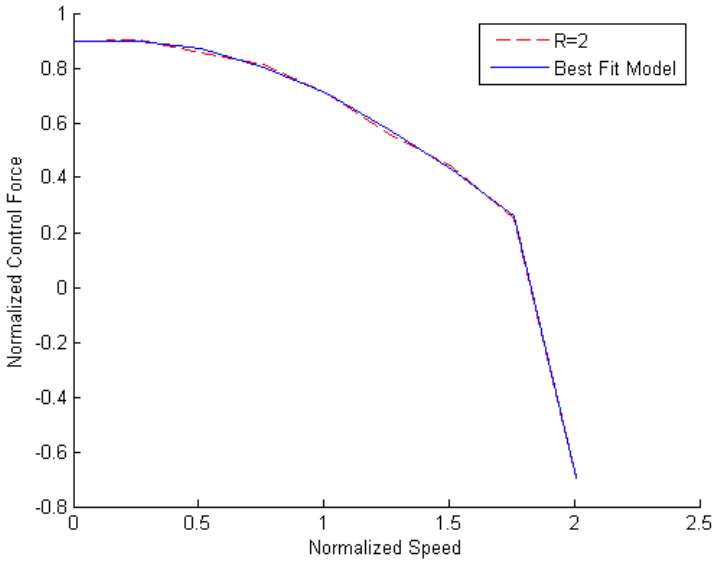

Fig. 19. Best fit of $\tilde{f}(v)$ curve for speeds less than critical speed

The Runge-Kutta method integrates the FONC in the simulation using this best-fit expression for $f(v)$. In Figures (20) - (22), it is seen that the disc speed for the approximation and true (best-fit) nonlinear solutions is not identical. However, this offset in disc speed does not affect either the control force or derivative of the control force. These results indicate that the control force calculated is accurate using either the full nonlinear solution or the linear solution found by using an approximated $f(v)$.

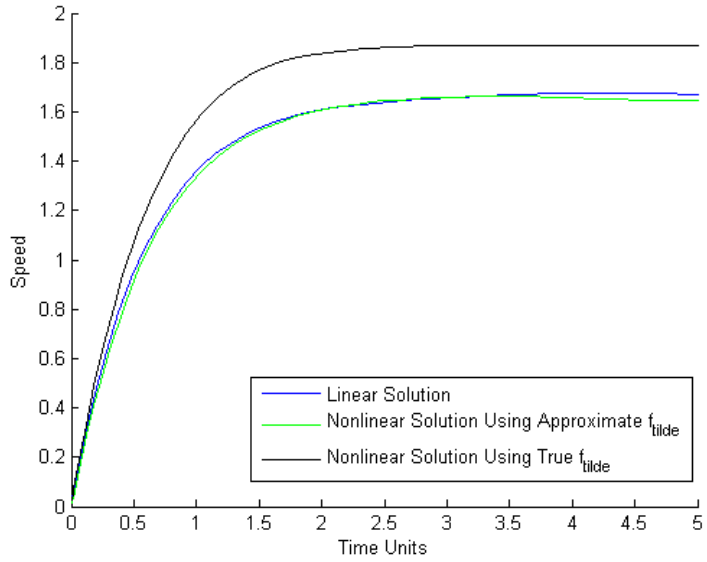

Fig. 20. Comparison of all solutions for disc speed

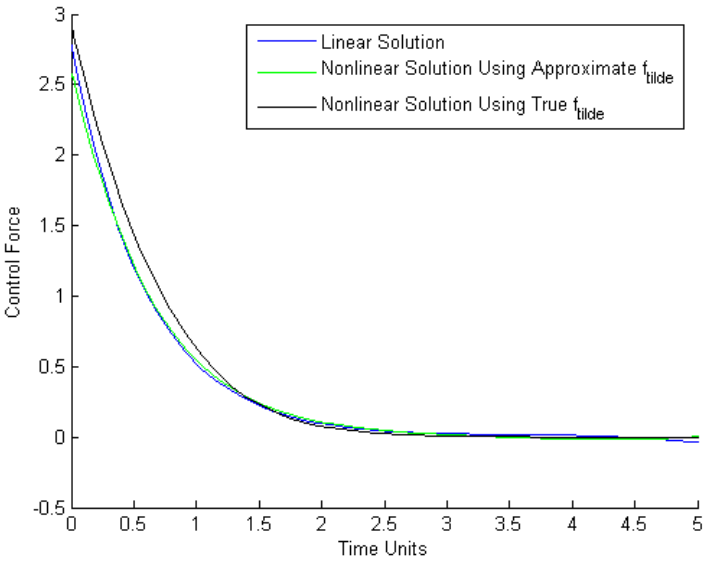

Fig. 21. Comparison of all solutions for control force

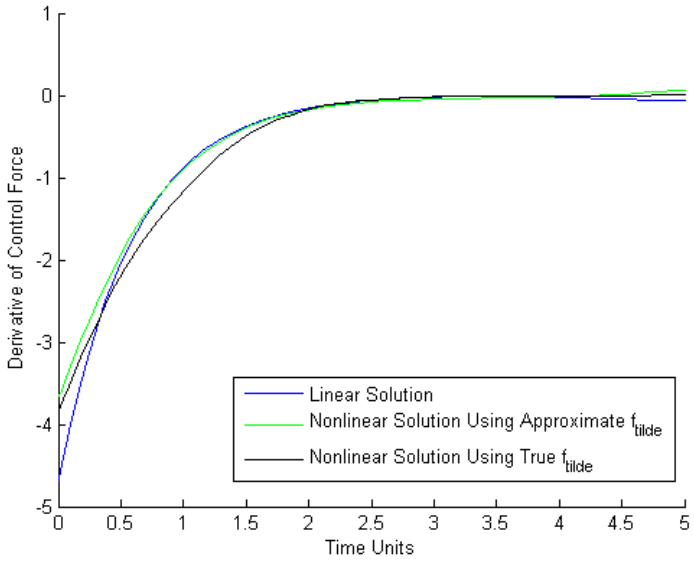

Fig. 22. Comparison of all solutions for derivative of control force

As longer iteration times are used, the linear and nonlinear curves become unstable; however, these long integration times are not practical when describing the coverage disc motion for a short time horizon. Small corrections in the near future could be taken to avoid these unstable conditions at a distant time. It is important to note that a simple feedback control law would be useful in designing such an imaging system.

3. FONC for Optimal Overlap

Consider a coverage disc traveling along the x-axis, partially overlapping a path covered by a previously moving disc. Figure (23) shows this scenario. Darker shades of gray correspond to higher values of Γ on the top portion of the figure. Note that within the currently moving coverage disc, $\Gamma \approx 1$ is achieved; however, this region is shown in white to emphasize the shaded partial coverage of the previous track. It is obvious from observation that a disc with partial coverage at its boundaries could

overlap with the partially-covered boundary of a previous path to accumulate full coverage in the overlap. This method does not require full coverage of the entire coverage disc's interior in any given pass.

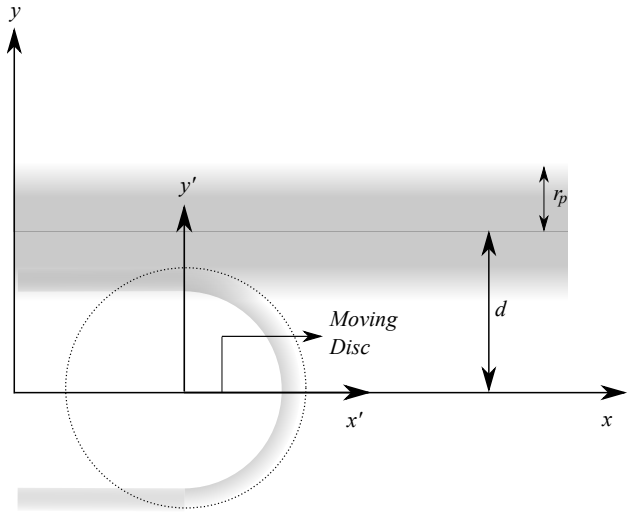

Fig. 23. Overlap of partially covered regions

The current coverage disc is traveling at the critical speed:

$$\bar{v} = v_c \tag{5.43}$$

which is used to calculate

$$\vec{\chi} = \bar{v}t \tag{5.44}$$

Assume that no velocity transients exist at the initial time. For various levels of overlap, the un-weighted pseudo-force, $\vec{f}(t)$, will now be compared. Recall from equation (4.24),

$$\vec{f}(t) = -\int_t^\infty d\tau\, e^{(-\tau-t)/T_h} \int_{D_R} du\, H'\big(\Gamma(\vec{u},\tau)\big)\Gamma^{R-1}(\vec{u},\tau)\vec{G}\big(\vec{u}-\vec{\chi}(t)\big) \tag{5.45}$$

Next, assign a coordinate system whose origin is always at the moving disc's center by defining an expression similar to that used in the derivation for the time-dependent velocity equations:

$$\vec{u}' = \vec{u} - \hat{x}\bar{v}(t)t \tag{5.46}$$

$$= y'\hat{y} + x\hat{x} \tag{5.47}$$

and

$$\tau' = \tau - t. \tag{5.48}$$

Using these two definitions, the unweighted pseudo-force and gradient function may be rewritten:

$$\vec{f}(t) = -\int_0^\infty d\tau'\, e^{-(\tau')/T_h} \int_{D_R} d^2u\, H'\big(\Gamma(\vec{u}', \tau')\big)\Gamma^{R-1}(\vec{u}', \tau')\vec{G}(\vec{u}') \tag{5.49}$$

$$\vec{G}'(\vec{u}') = -\delta(r - r_p)\big(cos\theta\hat{x} + \hat{y}sin\theta\big) \tag{5.50}$$

Equation (5.50) is substituted directly into equation (5.49), and the sifting property is then applied to yield

$$\vec{f}(t) = r_p \int_0^\infty d\tau'\, e^{-\tau'/T_h} \int_{D_R} du\, H'\big(\Gamma(\theta, \tau')\big)\Gamma^{R-1}(\theta, \tau')\Big(cos\theta\hat{x} + sin\theta\hat{y}\Big) \tag{5.51}$$

Now, Γ depends on the quantity $\tau' = \tau - t$. Let $\bar{\Gamma}$ be the coverage of the existing track, Γ_t be the coverage of the currently traveling disc, and Γ be the total coverage over both the previous and current track:

$$\bar{\Gamma} = \frac{2}{\bar{v}}\sqrt{r_p^2 - (y' - d)^2} \tag{5.52}$$

$$\Gamma_t = \begin{cases} min\left[\tau', \frac{2r_p cos\theta}{\bar{v}}\right]; & cos\theta \geq 0 \\ \frac{2|cos\theta|}{\bar{v}}; & cos\theta < 0 \end{cases} \tag{5.53}$$

The total value of Γ is,therefore, equal to

$$\Gamma = \Gamma_t + \bar{\Gamma} \tag{5.54}$$

$$= \frac{2}{\bar{v}}\sqrt{r_p^2 - (y' - \delta)^2} + \begin{cases} min\left[\tau', \frac{2r_p cos\theta}{\bar{v}}\right]; & cos\theta \geq 0 \\ \frac{2|cos\theta|}{\bar{v}}; & cos\theta < 0 \end{cases} \tag{5.55}$$

and would result in the optimum achievable cost for full coverage of the resolution disc.

C. Heuristic Comparison of Coverage Algorithms

So far, given a stationary initial position, which is unstable, one solution was shown for the unstable motion in the form of a rectilinear path. However, from observing the greater efficiency of overlapping paths, another type of unstable motion may exist. Rather than attempting to find a solution of the FONC, a spiral motion is devised with a few adjustable parameters, then these parameters are optimized by directly computing the cost function. Furthermore, simulations will be shown to give a heuristic comparison between coverage discs that follow a linear path and a spiral path; no dimensional units are defined for values in this simulation. The comparison is quantified using the cost function, which is composed of a thrust cost and a coverage cost. Recall from equation (3.16) that the cost is defined as

$$J = \int_0^{\infty} e^{-t/T_h} \left[\int_0^{D_R} d\vec{u} \left[1 - H\left(\Gamma^R(\vec{u}, t) \right) \right] + \mu \sum_{k=1}^{N} \left| \vec{T}_k \right|^2 \right] dt \tag{5.56}$$

The coverage penalty is measured using the first portion of the cost function, while the thrust penalty is defined as the second part of the cost governed by the summation. The total cost will be used to compare two different coverage strategies in the following two sections.

D. Coverage Algorithms

The two coverage algorithms investigated were a simple rectilinear path and spiral. Figures (24) and (25) show these two methods as simulated in the frequency plane in the left half portion of the figures. The corresponding motion of the spacecraft is shown in the right half of these figures as seen in the spatial plane.

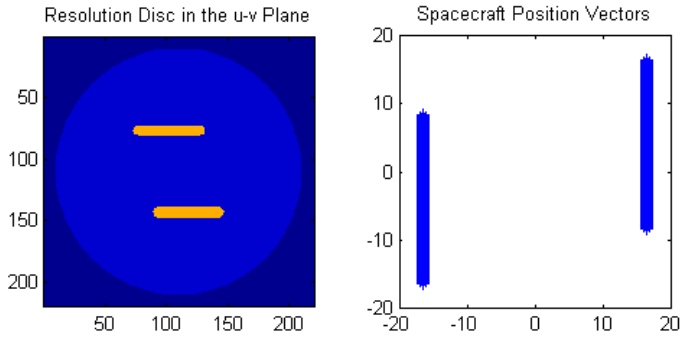

Fig. 24. Rectilinear coverage strategy in (left) frequency plane and (right) spatial plane

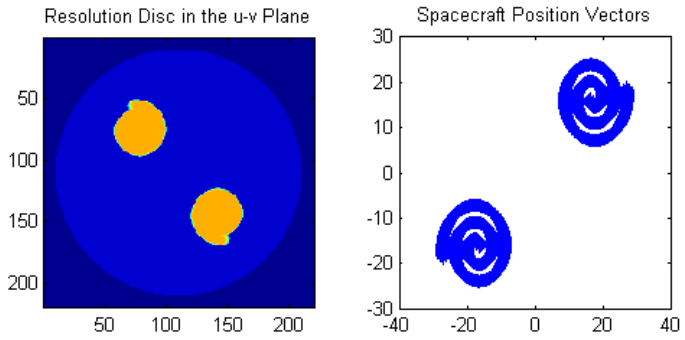

Fig. 25. Spiral coverage strategy in (left) frequency plane and (right) spatial plane

E. Results

Several simulations show that the cost for the rectilinear was more than that of the spiral maneuver for the same values of R and μ. Figure (26) shows an example of this comparison, and other values of μ and R showed the same trend. This difference in the cost is due to the fact that the spiral maneuver covers partially covered areas with another partial coverage path on the next encirclement. Contrastingly, the rectilinear motion does not achieve full coverage for any partially covered areas. Because this spiral motion is not driven by the first-order necessary conditions, more partial coverage overlap would be achieved by an optimal maneuver following these conditions.

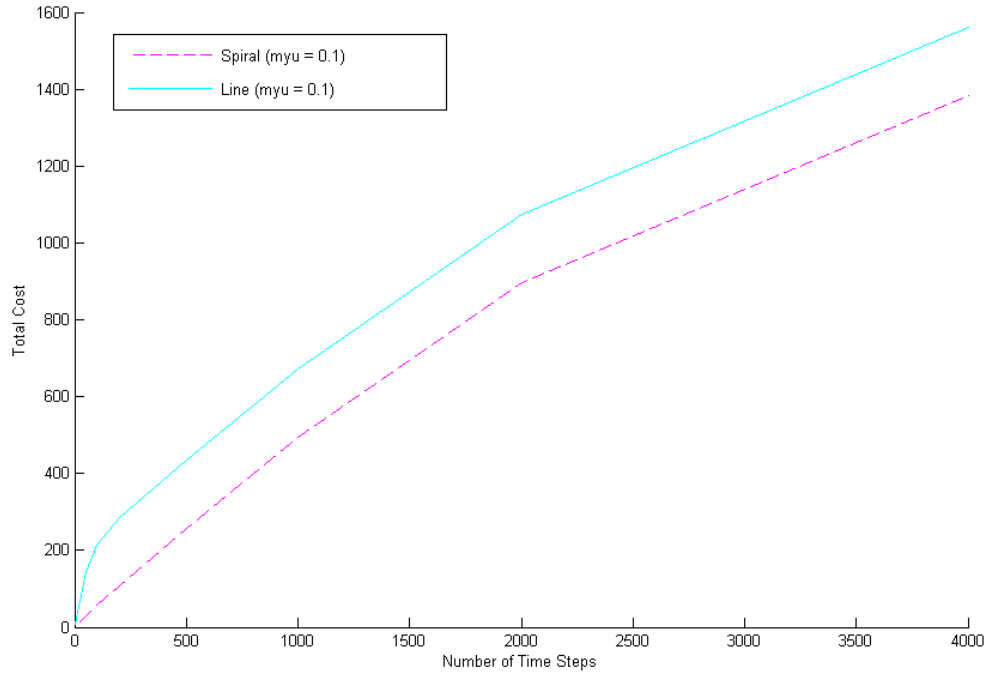

Fig. 26. Comparison of cost for two coverage strategies ($\mu = 0.1$)

Lower values of the weight, μ, were shown to correspond to lower values of the total cost, as emphasized in Figure (27). This figure again shows, in general, a lower cost for the spiral maneuver than the rectilinear maneuver.

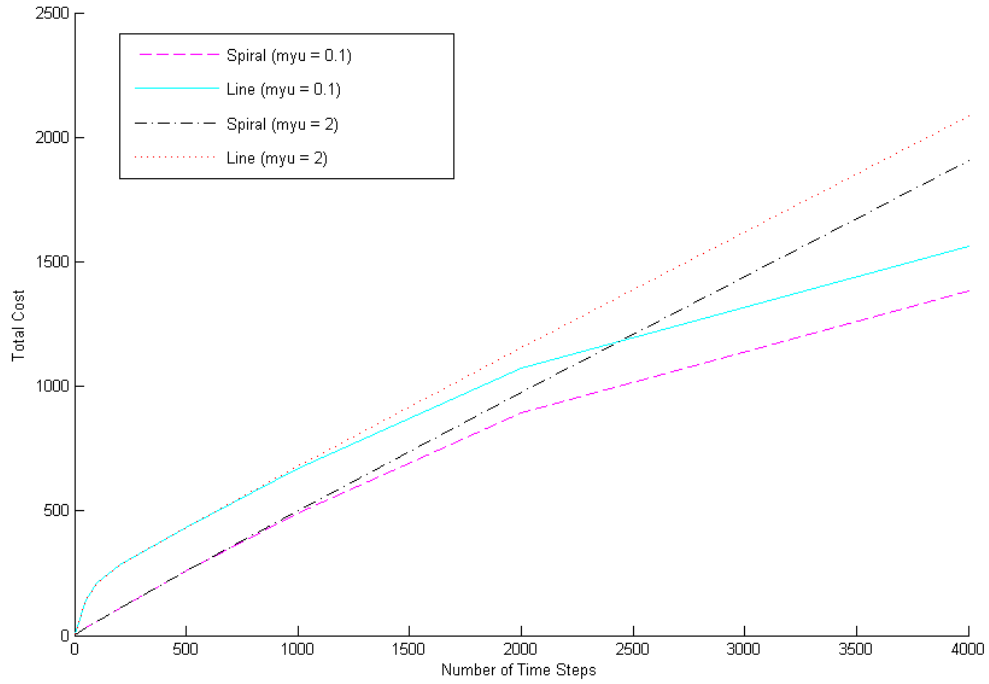

Fig. 27. Comparison of cost for different weights

The results also show that for the spiral maneuver, lower values of the risk exponent, R, give a lower value for the total cost, as seen in Figure (28). However, as shown in Figure (29), the value of R for rectilinear motion has no effect on the total cost.

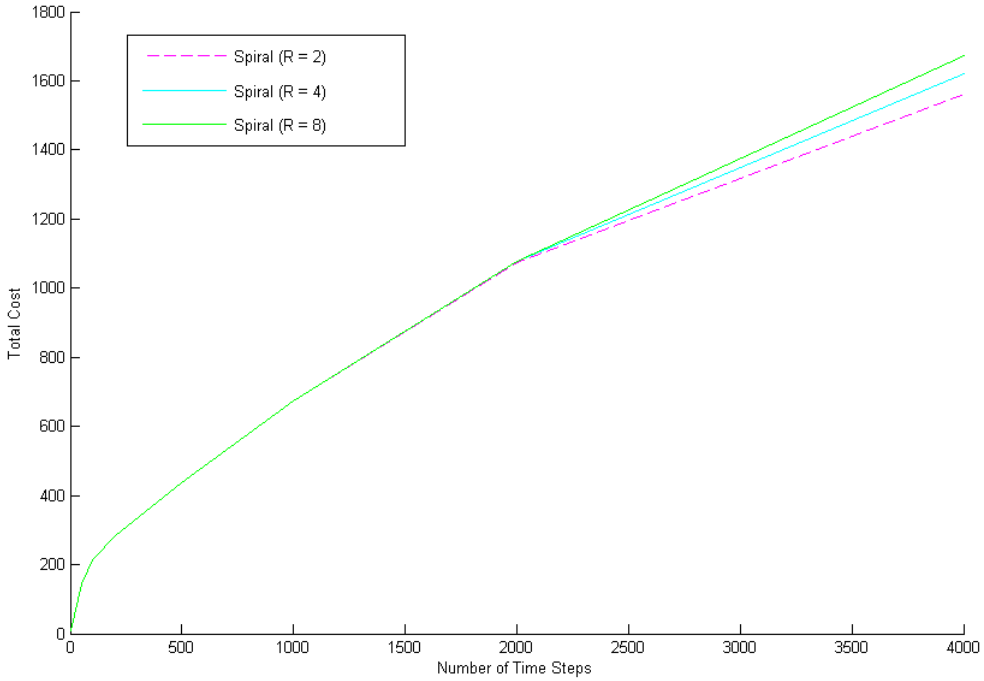

Fig. 28. Spiral maneuver comparison of cost for values of R

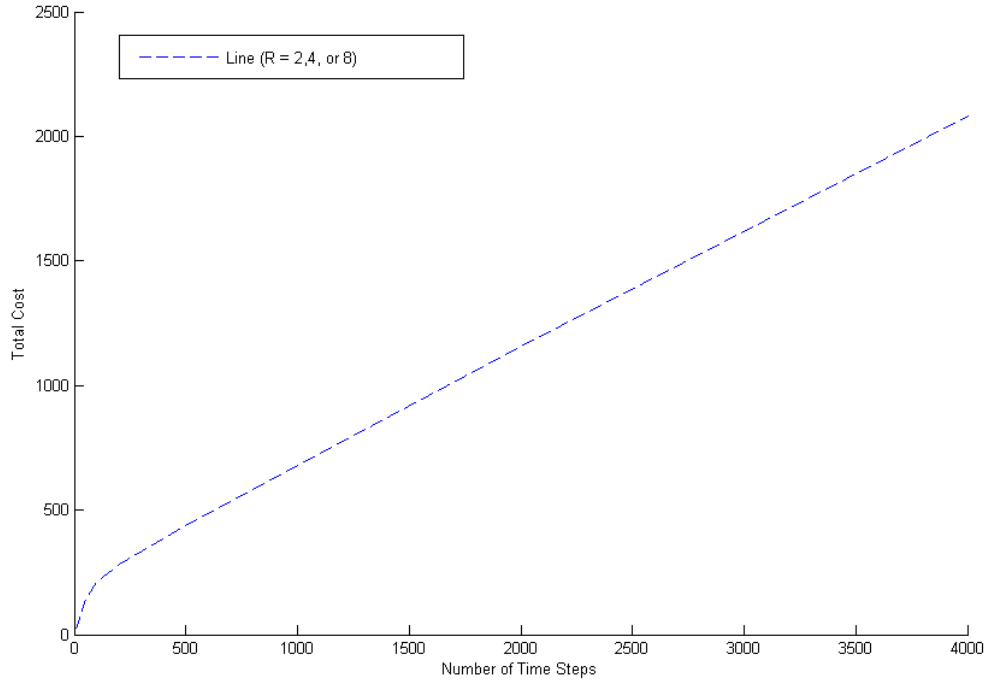

Fig. 29. Rectilinear maneuver comparison of cost for values of R

Figure (30) shows that the spiral maneuver gives a lower value for the total cost for time step greater than approximately 1000, regardless of the value of the risk exponent.

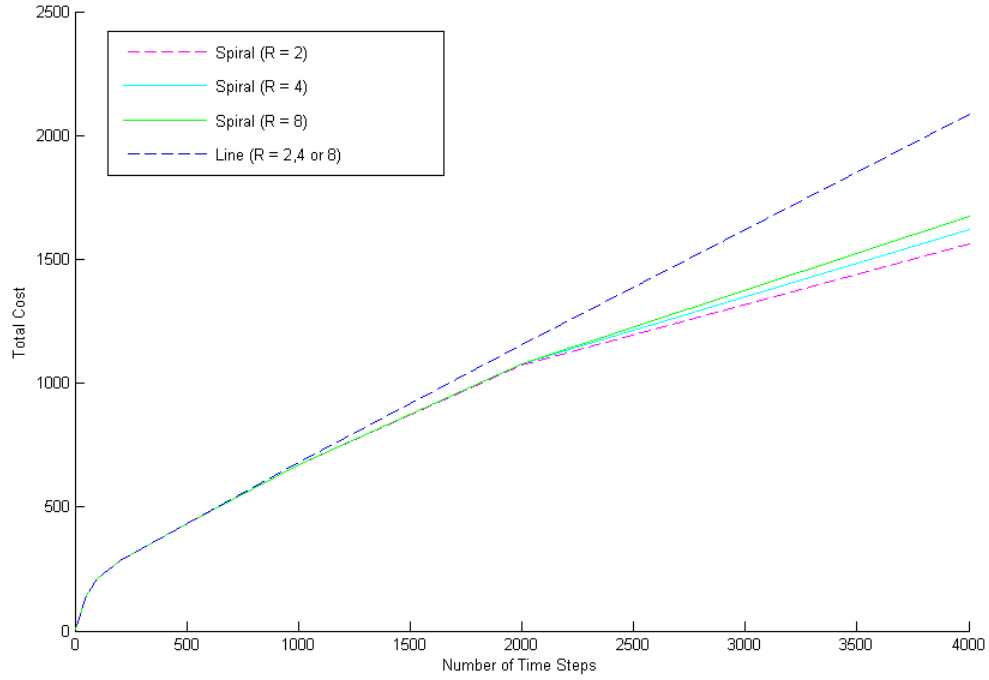

Fig. 30. Comparison of cost for values of R ($\mu = 2$)

The results of the heuristic comparison so far have shown that the spiral maneuver is much more efficient as indicated by the total cost function. However, this maneuver becomes less efficient than the rectilinear motion for large values of μ as the spiral's radius increases. In the same simulation that was used to generate the previous figures comparing the two types of motion, a value of $\mu = 94$ was found to be the point where the two maneuvers have the same cost. When $\mu > 94$, the rectilinear motion is the best choice as its cost is less. Similarly, when $\mu < 94$, the spiral maneuver was found to have a smaller cost. Figure (31) shows the maneuvers when they have the same cost; Figure (32) gives an example where the rectilinear motion is more effective.

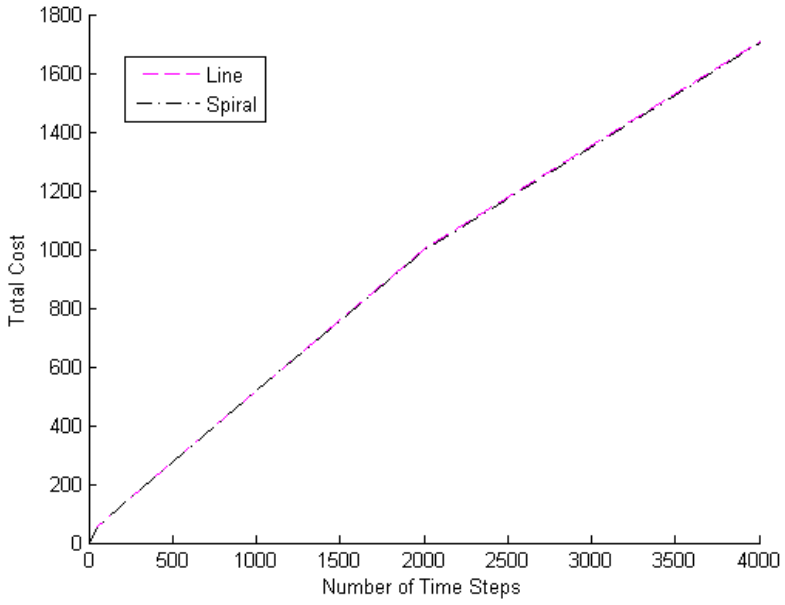

Fig. 31. Comparison of equivalent cost($\mu = 94$, $R = 8$)

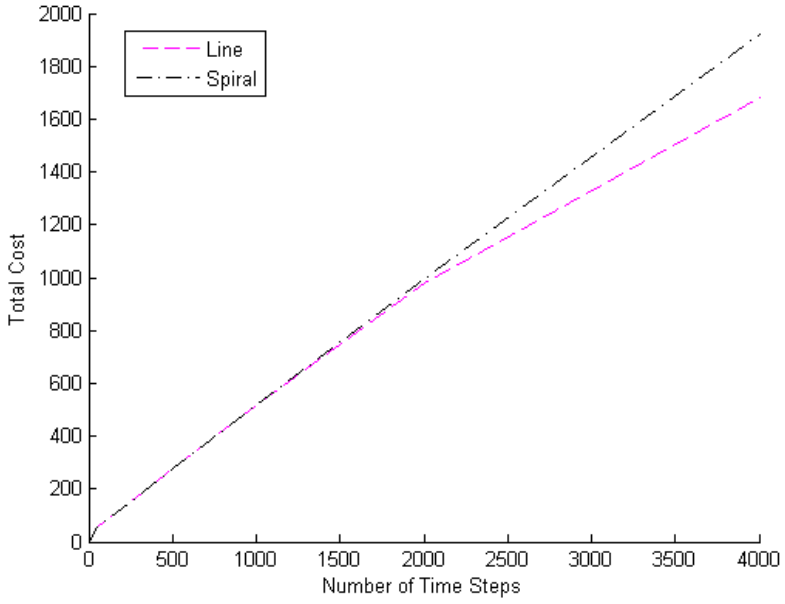

Fig. 32. Comparison of cost for large weights ($\mu = 100$, $R = 8$)

F. Summary

This chapter first showed the derivation for a projection from the spacecraft positions to coverage areas in the frequency plane. This projection was used for simulation purposes to ensure the center of mass was at the origin of the system. Next, the time-dependent velocity equations derived in Chapter IV were shown to match closely with the results of [2].

The FONC for one-dimensional motion were simplified and linearized; these equations were used to solve the two-point boundary problem. The solution was plotted and shown to behave as an expression composed of exponential functions, which would allow for a simple feedback control law to be implemented.

The conditions and equations for optimal overlap were given. The optimal overlap is based partly on the coverage disc's speed during the previous and current paths as well as an angle describing the location of a point within the disc.

In determining the most effective manner to cover the resolution disc, multiple strategies were used for the coverage disc motion. Straight line motion along the x-axis and spiral motion were implemented for a short time horizon approximation. Comparing the cost functions gave insightful results. Lower values of μ give a lower total cost; also, spiral motion proved to have a smaller cost than the rectilinear motion, regardless of the value of R. When μ became large, the rectilinear motion had a smaller cost than the spiral motion. The cost for the spiral maneuver could be further reduced by implementing the first-order necessary conditions such that an optimal overlap is achieved for the critical speed. However, developing simulations for these optimal conditions would be much more challenging than that for the heuristic approach described here and is beyond the scope of this study.

CHAPTER VI

CONCLUSIONS

This research explored methods for interferometric imaging of distant objects using multiple space-borne apertures. While this area of study is vast and mostly unexplored, investigating specialized cases and using simplifications gave insight into the behavior of such systems. The study expanded upon the previous research of [2], which was summarized to give a foundation for the current results.

Because an optimal solution for the proposed problem is challenging and will require much research before a complete solution is reached, simplified one-dimensional analysis methods were used. First, expressions were derived for coverage disc motion assuming a non-constant velocity that were used to solve the FONC two-point boundary problem. The results matched closely with that of [2], which assumed a constant velocity and neglected the initial velocity of $v(0) = 0$. A thin paintbrush metaphor was used for this time-dependent velocity approach to aid in visual understanding.

Next, a derivation used for simulation purposes was given to ensure that the control forces always meet given acceleration constraints. A projection was used for the Matlab simulations, where the center of each coverage disc was calculated based on the corresponding physical spacecraft positions.

A simplified equation for the un-weighted pseudo-force and its linearized expression were then derived and integrated forward in time to solve the FONC two-point boundary problem. These two solutions were shown to match closely over time. In both cases, the disc speed exponentially approached the critical speed of $v_c = 2$, while the control force and derivative of the control force exponentially approached zero as expected. These results were again achieved using a best-fit approximation equation

for the un-weighted pseudo-force. The results showed that a simple feedback law could be implemented to control the system, even when the estimated critical speed is not exact.

The conditions for optimal overlap in rectilinear coverage disc motion were given in terms of an image quality parameter, Γ. This optimal overlap is a function of the coverage disc's velocity and angle as measured from the axis of motion.

Lastly, a heuristic comparison between two types of coverage disc motion was given based on the value of the cost function. The spiral maneuver was shown to be a more efficient coverage strategy than the rectilinear motion. The results gave implications for a global maneuver that should be the goal of future work. Other future work could implement the optimal overlap conditions to verify that these results are correct. Additional special cases of general coverage disc motion could also be explored, such as overlapping rectilinear motion.

REFERENCES

[1] J. Riberos, "Design of fuel optimal maneuvers for multi-spacecraft interferometric imaging systems," M.S. thesis, Texas A&M University, College Station, Texas, August 2006.

[2] H. Al-Twaijry, "Multi-spacecraft optimal interferometric imaging," Ph.D. dissertation, University of Michigan, Ann Arbor, Michigan, 2006.

[3] I.I. Hussein, D.J. Scheeres, and D.C. Hyland, "Optimal formation control for imaging and fuel usage," Paper Presented at AAS Space Flight Mechanics Meeting, Copper Mountain, Colorado., 2005.

[4] M. Faucherre, F. Merkle, and F. Vakili, "Beam combination in aperture synthesis from space Field of view limitations and (u,v) plane coverage optimization," *New Technologies for Astronomy: SPIE*, vol. 1130, pp. 138–145, 1989.

[5] J. Leitner, "Formation flying - the future of remote sensing from space," *Proceedings of the 18th International Symposium on Space Flight Dynamics (ESA SP-548)*, pp. 621–626, October 2004.

[6] A. Labeyrie, S.G. Lipson, and P. Nisenson, *An Introduction to Optical Stellar Interferometry*, Cambridge University Press, Cambridge, United Kingdom, 2006.

[7] R. Sandau, "Distributed satellite sytems for earth observation and surveillance," *NATO Research and Technology Organization: Systems Concepts and Integration Panel Lecture Series*, April 2009.

[8] D.C. Hyland, "Entry pupil processing approaches for exo-planet imaging," *SPIE*, vol. 5905, August 2005.

[9] Goddard Space Flight Center, "Formation flying: The afternoon a-train satellite constellation," The Earth Science Enterprise Series., March 2003.

[10] L. Penin, J. Araújo, and N. Ávila, "Design and evaluation of optimal reconfiguration maneuvers for separated space interferometry," *Acta Astronautica*, vol. 57, pp. 330 – 340, April 2005.

[11] P.K.C. Wang and F.Y. Hadaegh, "Coordination and control of multiple microspacecraft moving in formation," *The Journal of the Astronautical Sciences*, vol. 44 (3), 1996.

[12] R. W. Beard, J. Lawton, and F.Y. Hadaegh, "A coordination architecture for spacecraft formation control," *IEEE Transactions on Control Systems Technology*, vol. 9 No. 6, November 2001.

[13] M. Reyhanoglu and D. Dyer, "Control system design and simulation of spacecraft formations," *in Industrial Electronics, IECON. 34th Annual Conference of IEEE*, pp. 120 - 125, 2008.

[14] S. D'Amico and O. Montenbruck, "Proximity operations of formation-flying spacecraft using and eccentricity/inclination vector separation," *Journal of Guidance, Control, and Dynamics*, vol. 29 No. 3, pp. 554 – 563, May - June 2006.

[15] D.C. Hyland, "Efficient, passively orbiting constellations for high resolution imaging of geosynchronous objects," in *Astrodynamics Specialist Conference*, Mackinac Island, Michigan, August 2007, AAS/AIAA, pp. 811 - 828.

[16] E. Wolf and M. Born, *Principles of Optics*, Pergamon Press, Ltd., Oxford, England, 1959.

[17] P. Haraharan, *Basics of Interferometry*, Elsevier, Inc., Burlington, Massachusetts, 2nd edition, 2007.

[18] E. Hecht, *Optics*, Pearson Education, Inc., San Francisco, California, 4th edition, 2002.

[19] J.F. James, *A Student's Guide to Fourier Transforms with Applications in Physics and Engineering*, Cambridge University Press, Cambridge, United Kingdom, 2 edition, 2004.

[20] O.K. Ersoy, *Diffraction, Fourier Optics, and Imaging*, A John Wiley & Sons, Inc., Hoboken, New Jersey, 2007.

[21] R. Hanbury Brown, "Measurement of stellar diameters," *Annual Review of Astronomy and Astrophysics*, vol. 6, pp. 13, 1968.

VITA

Julie Sandberg attended the University of Wyoming, where she earned her Bachelor of Science in Electrical Engineering in 2007. During her undergraduate career, Julie held several internships at NASA's Jet Propulsion Laboratory and Goddard Space Flight Center, as well as Ball Aerospace & Technologies Corp. She then earned her Master of Science degree in Aerospace Engineering at Texas A&M University in 2010. Her interests are in dynamics & control, digital signal processing, and programming microcontrollers. Julie may be contacted at the following address:

Texas A&M University
Department of Aerospace Engineering
H.R. Bright Building, Rm. 701, Ross Street - TAMU 3141
College Station TX 77843-3141